UNICA
UNIVERSITÀ
DEGLI STUDI
DI CAGLIARI

This is the author's accepted manuscript version of the following contribution:

Bibinur Meirbekova, Michele Brun Control of elastic shear waves by periodic geometric transformation: cloaking, high reflectivity and anomalous resonances. *Journal of the Mechanics and Physics of Solids, 137, 103816, 2020*

© < 2020 >. This manuscript version is made available under the CC-BY-NC-ND 4.0 license

The publisher's version is available at:
https://doi.org/10.1016/j.jmps.2019.103816

When citing, please refer to the published version.

This full text was downloaded from iris
https://iris.unica.it/

Control of elastic shear waves by periodic geometric transformation: cloaking, high reflectivity and anomalous resonances

Bibinur Meirbekova[1,2] and Michele Brun*[1]

[1]Dipartimento di Ingegneria Meccanica, Chimica e dei Materiali, Università di Cagliari, 09123 Cagliari, Italy
[2]Department of Mechanics and Mathematics, Al-Farabi Kazakh National University, 050040 Almaty, Kazhakstan

Keywords: Metamaterials Geometric transformation Periodic cloaking Multipole expansion method Homogenisation High reflectivity Anomalous resonance

Abstract

A doubly periodic geometric transformation is applied to the problem of out of plane shear wave propagation in a doubly periodic perforated elastic medium. The technique leads to the design of a system of radially anisotropic and inhomogeneous shells surrounding the void inclusions, that can be tuned to give the desired filtering properties.

For a regular transformation, the transformed elastic system displays the same dispersion properties than the original homogeneous one, but for overlapping and unfolding transformations new filtering properties can be obtained, which include anomalous resonances at zero and finite frequencies. Low-frequency homogenisation reveals how it is possible to tune the phase and group velocity in the long-wave limit at any value, or to obtain a zero frequency band gap for Neumann boundary conditions. The dispersion properties of the medium are studied both semi-analytically by the multipole expansion and numerically by the finite element methods.

Several applications are shown, including the transmission problem throughout a grating of void inclusions and an interface in a waveguide, where the capability of

*Corresponding author

the proposed model is quantitatively demonstrated by computing the transmitted power flow. Finally, we gave a demonstration of defect modes in a waveguide and of tuning the transformation for the research of Dirac points.

Keywords: metamaterials, geometric transformation, periodic cloaking, multipole expansion method, homogenisation, high reflectivity, anomalous resonance.

1 Introduction

Artificial made media, known as *metamaterials*, are well known nowadays for their exotic capabilities to manipulate wave propagation [16, 20, 83], including negative refraction [74, 94], spontaneous emission control [4, 67] and anomalous tunneling effects [19, 85]. Probably, the most famous application consists in the possibility to make an object invisible to an impinging wave, by placing it in a cloak having the capability to cancel the scattering induced by the object itself. The research of invisibility dates back to previous centuries [31, 34, 46] and interesting models were also proposed in elasticity, including a coated elastic hole that, under specific external loads, does not perturb the static field [44], the coated sphere assemblage for hydrostatic loads [30, 43] and the energetically neutral inclusion covered by a structural interface [7].

Nevertheless, it was with the advent of metamaterials that the attention on the topic reached a vast community. Active and passive cloaks are applied to hide an object. An active cloak consists of a set of discrete multipole sources distributed in space to destructively interfere with an incident time-harmonic waves so as to nullify the total field in some finite domain and ensure that, in the far field, only the incident wave is present. The idea, which takes inspiration from active control of sound [42, 62], was applied

to electromagnetism [91, 92], acoustics [69, 93], vector elasticity [70] and flexural waves in thin plates [73].

Passive systems are based on geometric transformation techniques, where a simply connected region, most often a circle, is mapped into a multiply connected one (an annulus). In the past conformal mappings, which are locally non deviatoric transformations, were frequently used to solve plane problems of mechanics [36, 60], with the possibility to take advantage of the properties of complex variable. Greenleaf, Lassas an Uhlmann [28, 29] showed that singular transformations could lead to cloaking for conductivity, while [76] and [37] made the key observation that singular transformations could be used to achieve cloaking of electromagnetic waves. A regular transformation was proposed in [15, 35] where a small, but finite central simply connected domain is transformed into a larger one. The theory for acoustic cloaking is presented in [68], where, instead of the differential geometry formalism, a formulation adapted from the theory of finite elasticity was adopted. For problems governed by the Helmholtz equation the transformed equation can be associated to an inhomogeneous and anisotropic material.

In vector elasticity, the wave equations are not invariant under a general mapping [10, 52, 71], since either non-symmetric stress or tensorial density are required. In this case, it was shown that the modified Newton's second law [55] remains invariant under specific conditions. The biharmonic equation for flexural wave propagation in Kirchhoff plates is transformed into an equation of an inhomogeneous and anisotropic plate in presence of in-plane stress [9, 14] usually studied in problems of static buckling of plates.

Cloaking of a finite number of inclusions were considered in [3, 56] for the electromagnetic and flexural wave propagation, respectively.

Extended reviews on transformation optics in metamaterials in different fields, with a focus on experimental results, can be found in [24, 32, 82].

In this work, transformation optics techniques are applied periodically on a periodic system. Propagation of out of plane shear waves in linear elastodynamics is considered. An illustrative example in Figure 1 shows the capability of the system to cloak multiple void inclusions of relatively large size. By making use of the periodicity it is possible to cloak not only a single inclusion but a grating and, in addition, high reflective systems and multiple anomalous localised resonances [54, 64–66] can be obtained.

The focus is initially on the comparative analysis of dispersive properties of the transformed and original systems. To analyse the dispersive properties, we implemented both finite element codes and the semi-analytical multipole expansion method. Concerning the multipole expansion method, the solution of the incident and scattered fields for a single obstacle can be found in [72], while dispersion properties in an infinite one-dimensional array and doubly periodic arrays of circular scatterers were carried out in [96] for out of plane shear waves and in [47, 59, 78, 79] for flexural waves in Kirchhoff plates. Arbitrarily shaped obstacles were considered in [87, 88].

The paper is organized as follows. In Section 2 we present initial and transformed equations of motion and corresponding boundary conditions, describing the periodic locally radial geometric transformation. In Section 3 we report the comparative analysis

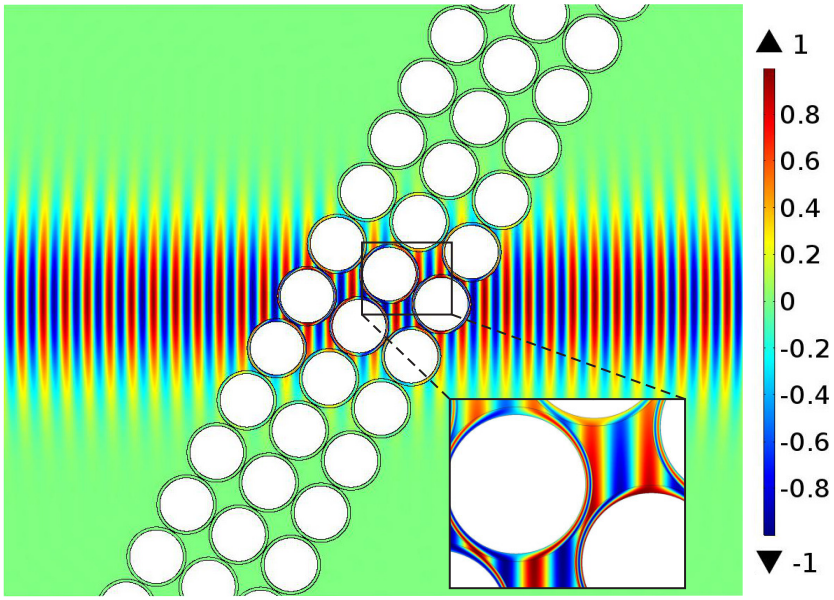

Figure 1: Wave transmission of a Gaussian beam throughout a slab of void inclusions. Each void is surrounded by a cloaking interface. Displacement distribution is shown, details on the computation are reported in Section 4.1. (For interpretation of the references to colour, the reader is referred to the web version of this article.)

of dispersion properties and briefly describe the applied multipole expansion method. In particular, we focus our attention on classical, overlapping and unfolding transformations by also performing a low-frequency, long wavelength homogenisation. In Section 4 we show several applications including a transmission problems in a continuum and in a waveguide, the detection of defect modes and the design of the transformation for the existence of Dirac points. Final consideration are given in last Section.

2 Out of plane shear waves in a doubly periodic medium

We consider the doubly periodic medium shown in Figure 2a, it consists of a square distribution of cylindrical holes of radius R_1.

The centers of the holes in each unit cell have the position

$$\mathbf{Y^h} = h_1\mathbf{a}_1 + h_2\mathbf{a}_2, \qquad \mathbf{a}_1 = \begin{pmatrix} d \\ 0 \\ 0 \end{pmatrix}, \ \mathbf{a}_2 = \begin{pmatrix} 0 \\ d \\ 0 \end{pmatrix}, \tag{1}$$

where d is the dimension of the edge of the unit cell and $\mathbf{h} = (h_1, h_2)^T$, with $h_1, h_2 \in \mathbb{Z}$, a multi-index.

2.1 Governing equations

We analyze wave propagation in the time-harmonic regime, the time dependence $e^{-i\omega t}$, with ω the radian frequency and t the time, is not indicated for ease of notation. We focus on out of plane shear waves, the displacement is

$$\mathbf{U} = \begin{pmatrix} 0 \\ 0 \\ U(\mathbf{X}) \end{pmatrix}, \tag{2}$$

where $\mathbf{X} = (X_1 \ \ X_2 \ \ 0)^T$ is the position vector.

Wave propagation in a linear elastic medium is governed by the Helmholtz equation [27]

$$\nabla_{\mathbf{X}} \cdot \mathbf{C}^{(0)} \nabla_{\mathbf{X}} U(\mathbf{X}) + \rho_0 \omega^2 U(\mathbf{X}) = 0, \qquad \text{for } \mathbf{X} \in \Omega_{R_1,d}, \tag{3}$$

where $\mathbf{C}^{(0)}$ is the second-order stiffness tensor for out of plane motion[1], ρ_0 the density and $\nabla_{\mathbf{X}}$ the gradient operator in the original domain. The domain

$$\Omega_{R_1,d} = \mathbb{R}^2 \setminus \Omega'_{R_1,d}, \tag{4}$$

[1]With respect to the full fourth-order stiffness tensor $\mathcal{C}^{(0)}$, we have $C^{(0)}_{ij} = 2\,\mathcal{C}^{(0)}_{i3j3}$, where $i, j = 1, 2$ in cartesian coordinates and $i, j = R, \Theta$ in cylindrical ones.

where the complement

$$\Omega'_{R,d} = \bigcup_{h_1,h_2=-\infty}^{+\infty} S(\mathbf{Y^h}, R), \quad \text{with} \quad S(\mathbf{Y^h}, R) = \{\mathbf{X} : |\mathbf{X} - \mathbf{Y^h}| < R\}. \tag{5}$$

For later use we also define

$$Q(\mathbf{Y^h}, d) = \{\mathbf{X} : 0 \leq X_1 - Y_1{}^{\mathbf{h}} \leq d,\ 0 \leq X_2 - Y_2{}^{\mathbf{h}} \leq d\}, \tag{6}$$

so that the domain of the generic unit cell is

$$\Omega^{\mathbf{h}}_{R_1,d} = \overline{Q(\mathbf{Y^h}, d)} \setminus S(\mathbf{Y^h}, R_1), \tag{7}$$

where the bar indicates the closure.

The linear momentum balance (3) is complemented by either Neumann or Dirichlet boundary conditions on $\partial\Omega_{R_1,d}$, namely

$$\mathbf{C}^{(0)}\nabla_{\mathbf{X}} U(\mathbf{X}) \cdot \mathbf{n} = \mathbf{0} \quad \text{or} \quad U(\mathbf{X}) = \mathbf{0}\,. \tag{8}$$

For an isotropic medium, eqn. (3) reduces to the classical Helmholtz equation

$$\Delta_{\mathbf{X}} U(\mathbf{X}) + \beta^2 U(\mathbf{X}) = 0, \qquad \mathbf{X} \in \Omega_{R_1,d}, \tag{9}$$

with $\beta = \omega/c_0$ the frequency parameter, $c_0 = \sqrt{\mu_0/\rho_0}$ the phase velocity, μ_0 the shear modulus and $\Delta_{\mathbf{X}}$ the Laplacian operator in the original domain. The associated Neumann boundary conditions are

$$\mu_0 \nabla_{\mathbf{X}} U(\mathbf{X}) \cdot \mathbf{n} = \mathbf{0} \quad \text{on} \quad \partial\Omega_{R_1,d}\,, \tag{10}$$

while Dirichlet conditions remain as in (8).

2.2 Transformed Geometry

A radial geometric transformation is applied in each unit cell: the shell centred at $\mathbf{Y^h}$, with internal and external radii R_1 and R_0,

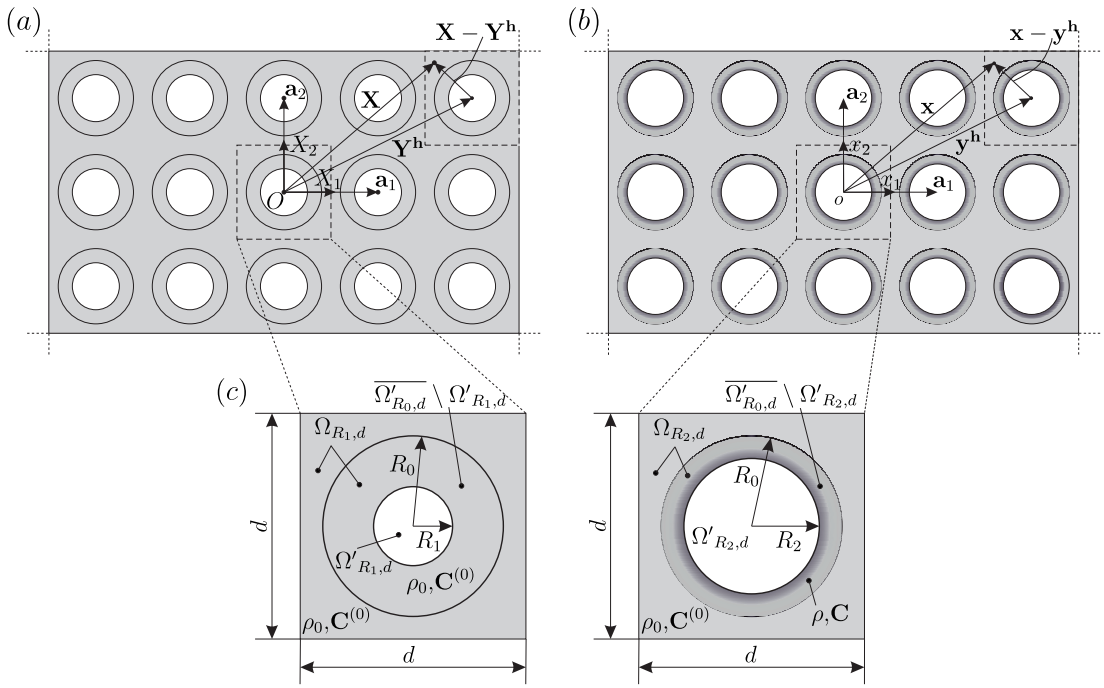

Figure 2: (a) Original and (b) transformed doubly periodic perforated domains. (c) Unit cells. The linear isotropic and homogeneous elastic material in the shell $R_1 < R < R_0$ is transformed into the linear anisotropic and inhomogeneous elastic material in the region $R_2 < r < R_0$.

respectively, is mapped into the shell centred at $\mathbf{y}^{\mathbf{h}} = \mathbf{Y}^{\mathbf{h}}$, with internal and external radii R_2 and R_0, respectively (see Figure 2c). The linear radial mapping $\mathbf{x} = \mathcal{F}(\mathbf{X})$, for $\mathbf{X} \in \overline{\Omega'_{R_0,d}} \setminus \Omega'_{R_1,d}$, in each cell is

$$\begin{cases} r^{\mathbf{h}} = g(R^{\mathbf{h}}) = R_0 + \alpha_1 (R^{\mathbf{h}} - R_0), \\ \theta^{\mathbf{h}} = \Theta^{\mathbf{h}}, \end{cases} \tag{11}$$

where

$$\alpha_1 = \frac{R_0 - R_2}{R_0 - R_1},$$

and

$$R^{\mathbf{h}} = |\mathbf{X} - \mathbf{Y}^{\mathbf{h}}|, \quad \Theta^{\mathbf{h}} = 2 \arctan\left(\frac{X_2 - Y_2^{\mathbf{h}}}{X_1 - Y_1^{\mathbf{h}} + R^{\mathbf{h}}} \right),$$

$$r^{\mathbf{h}} = |\mathbf{x} - \mathbf{y}^{\mathbf{h}}|, \quad \theta^{\mathbf{h}} = 2 \arctan\left(\frac{x_2 - y_2^{\mathbf{h}}}{x_1 - y_1^{\mathbf{h}} + r^{\mathbf{h}}} \right). \tag{12}$$

We stress that the transformed geometry maintains the same periodicity as the original one, but it can be easily expanded to non-periodic transformations. The inverse transformation $\mathbf{X} = \mathcal{F}^{-1}(\mathbf{x})$, for $\mathbf{x} \in \overline{\Omega'_{R_0,d}} \setminus \Omega'_{R_2,d}$, is

$$\begin{cases} R^{\mathbf{h}} = G(r^{\mathbf{h}}) = g^{-1}(r^{\mathbf{h}}) = R_0 + \dfrac{r^{\mathbf{h}} - R_0}{\alpha_1}, \\ \Theta^{\mathbf{h}} = \theta^{\mathbf{h}}. \end{cases} \tag{13}$$

2.3 Transformed equation of motion

Restricting the attention to the cell identified by $h_1 = h_2 = 0$, with $\mathbf{Y^0} = \mathbf{y^0} = \mathbf{0}$, the governing eqn. (3) is transformed into

$$\nabla \cdot \mathbf{C} \nabla u(\mathbf{x}) + \rho\, \omega^2 u(\mathbf{x}) = 0, \tag{14}$$

where $u(\mathbf{x})$ is the transformed displacement, that we assume equal to $U(\mathbf{X})$. In addition, ∇ is the gradient operator in the transformed domain and ρ and $\mathbf{C}$ the transformed density and stiffness tensor, respectively [15, 68]. They can be given in terms of the Jacobian of the transformation, which can be expressed in cylindrical coordinates as

$$\mathbf{F}(\mathbf{X}) = \begin{bmatrix} g'(R) & 0 \\ 0 & \frac{g(R)}{R} \end{bmatrix} = \begin{bmatrix} \frac{1}{G'(r)} & 0 \\ 0 & \frac{r}{G(r)} \end{bmatrix}, \tag{15}$$

where the superscript $^{\mathbf{0}}$ will not be indicated in the following for ease of notation. Thus,

$$\mathbf{C} = \frac{1}{J} \mathbf{F}\, \mathbf{C}^{(0)}\, \mathbf{F}^T, \;\; \rho = \frac{\rho_0}{J}, \tag{16}$$

with

$$J = \det \mathbf{F} = \frac{g'(R)\, g(R)}{R} = \frac{r}{G(r) G'(r)}. \tag{17}$$

The transformed Helmholtz eqn. (14) represents a linear anisotropic and inhomogeneous material. If $\mathbf{C}^{(0)}$ is isotropic, under transformation (11) the transformed material is radially anisotropic and the governing equation (14) takes the form

$$\frac{\partial^2 u}{\partial r^2} + \frac{G'(r)}{G(r)}\frac{\partial u}{\partial r} + \left[\frac{G'(r)}{G(r)}\right]^2 \frac{\partial^2 u}{\partial \theta^2} + [G'(r)\beta]^2 u = 0, \tag{18}$$

where

$$\frac{G'(r)}{G(r)} = \frac{R_0 - R_1}{R_0(R_1 - R_2) + r(R_0 - R_1)}, \qquad G'(r) = \frac{1}{\alpha_1} = \frac{R_0 - R_1}{R_0 - R_2}. \tag{19}$$

Note that, in the untransformed domain

$$\frac{G'(r)}{G(r)} = \frac{1}{r}, \qquad G'(r) = 1. \tag{20}$$

3 Dispersion properties

Here, we analyze dispersion properties for both original and transformed geometries. The dispersion properties have been computed both numerically, using the finite element package *Comsol Multiphysics 5.3*, and semi-analytically, implementing the multipole expansion method. The semi-analytical approach, while of more difficult implementation, shows in closed form the relationship between the dispersion properties of the original and transformed geometries and is used to obtain Dirac points through a recursive algorithm.

The multipole expansion method is fully detailed in [47, 79, 89]. For completeness, we briefly present the method in the following together with the application to the case of transformed geometry.

3.1 Multipole expansion method

The displacement is expressed by separation of variables. In the transformed geometry, the problem is governed by the equation of motion (18), and the displacement can be given by

$$u(r,\theta) = \begin{cases} \sum_{n=-\infty}^{\infty} \left[A_n^s J_n(\beta\, G(r)) + B_n^s H_n^{(1)}(\beta\, G(r))\right] e^{in\theta}\,, & \text{in } \overline{\Omega'_{R_0,d}} \setminus \Omega'_{R_2,d}\,, \\ \sum_{n=-\infty}^{\infty} \left[A_n^m J_n(\beta\, r) + B_n^m H_n^{(1)}(\beta\, r)\right] e^{in\theta}, & \text{in } \Omega_{R_0,d}\,. \end{cases} \tag{21}$$

In the shell domains $\overline{\Omega'_{R_0,d}} \setminus \Omega'_{R_2,d}$, $G(r)$ is as in eqn. (13). In (21) $H_n^{(1)} = J_n + iY_n$ is the Hankel function, J_n,Y_n are the Bessel functions of the first and second kind [1] and the unknown coefficients $A_n^{s,m}$, $B_n^{s,m}$ must be determined from the boundary and interface conditions. The superscripts m and s indicate the matrix and the shell domains.

The interface boundary conditions on $\partial\Omega_{R_0,d}$ ($r = R_0$), imposing continuity of displacements and shear tractions between the anisotropic shells and the isotropic matrix, imply that

$$A_n^m = A_n^s, \quad B_n^m = B_n^s, \qquad n \in \mathbb{Z}. \tag{22}$$

Neumann boundary conditions on $\partial\Omega_{R_2,d}$ ($r = R_2$, see Figure 2c) impose that

$$A_n^s = -\frac{H'^{(1)}_n(\beta G(R_2))}{J'_n(\beta G(R_2))} B_n^s, \qquad n \in \mathbb{Z}\,, \tag{23}$$

while quasi-periodicity conditions have been obtained from a Rayleigh identity [59, 81], giving

$$A_n^s = \sum_{l=-\infty}^{\infty} (-1)^{l-n} S^H_{l-n}(\beta, \mathbf{k}) B_n^s, \qquad n \in \mathbb{Z}\,. \tag{24}$$

In eqn. (24), $S^H_{l-n}(\beta,\mathbf{k}) = -\delta_{l,0} + iS^Y_l(\beta,\mathbf{k})$ is the lattice sum [6, 13, 21, 79], with δ the Kronecker delta and $k = |\mathbf{k}|$ the magnitude of the Bloch vector. In [58] different ways of evaluating the non-trivial lattice sum are reviewed. Here, we adopt the representation given by Chin et al. [13], obtained by repeated integration to accelerate convergence

$$S^Y_l(\beta,\mathbf{k}) = -\frac{1}{J_{l+q}(\beta\lambda)}\left(\left[Y_q(\beta\lambda) + \frac{1}{\pi}\sum_{n=1}^{q}\frac{(q-n)!}{(n-1)!}\left(\frac{2}{\beta\lambda}\right)^{q-2n+2}\right]\delta_{l,0} + \right.$$
$$\left. +4i^l \sum_{\substack{h_1,h_2=-\infty \\ \mathbf{h}\neq\mathbf{0}}}^{+\infty}\left(\frac{\beta d}{Q_\mathbf{h}}\right)^q \frac{J_{l+q}(Q_\mathbf{h}\lambda)}{Q^2_\mathbf{h} - (\beta d)^2} e^{il\eta_\mathbf{h}}\right) \quad (25)$$

where $\mathbf{Q_h} = (k_1 d + 2\pi h_1, k_2 d + 2\pi h_2)$ and $\eta_\mathbf{h} = \arctan(\mathbf{Q_h})$. The parameter λ is arbitrary and taken equal to d, the acceleration parameter q is typically chosen between 3 and 7 and, as shown in [59], increasing it makes the series converge more rapidly for large $Q_\mathbf{h}$, but delays the onset of rapide convergence; for our case, we took $q = 3$.

Notice that the singularities $Q^2_\mathbf{h} - \beta^2 = 0$ correspond to the dispersion equation of a homogeneous square array.

Eqns. (23) and (24) lead to the following system

$$\left[\sum_{l=-\infty}^{\infty}(-1)^{l-n} S^H_{l-n}(\beta,\mathbf{k}) J'_n(\beta G(R_2)) + H'^{(1)}_n(\beta G(R_2))\right] B^s_n = 0. \quad (26)$$

The system (26) has infinite dimension and is truncated at N to give the finite system

$$\mathbf{M}(\beta,\mathbf{k})\mathbf{B} = \mathbf{0}, \quad (27)$$

having dimension $(2N+1, 2N+1)$. The dispersion relation is

the characteristic equation

$$\det[\mathbf{M}(\beta, \mathbf{k})] = 0. \tag{28}$$

of the spectral problem (27).

For Dirichlet boundary conditions on $\partial\Omega_{R_2,d}$, first derivatives ${J'}_n$ and ${H'}_n^{(1)}$ are substituted by J_n and $H_n^{(1)}$ in eqns. (23) and (26).

In the original geometry, where the problem is governed by the equation of motion (9), the displacement is given in the form

$$U(R,\Theta) = \sum_{n=-\infty}^{\infty} \left[A_n J_n(\beta R) + B_n H_n^{(1)}(\beta R)\right] e^{in\Theta}. \tag{29}$$

The dispersion relation (28) is obtained following the procedure detailed in eqns. (23-28), where $G(R_2)$ is replaced by R_1 and A_n^s and B_n^s by A_n and B_n, respectively.

Dispersion surfaces have been computed fixing the wave vector $\mathbf{k}$ and searching for the frequencies satisfying the dispersion relation. A comparison between results obtained implementing the multipole expansion method and *Comsol Multiphysics* is reported in Appendix A.

3.2 Dispersion properties of transformed and untransformed domains

The dispersion properties of untransformed and transformed geometries are analysed here. In Figure 3, we compare the dispersion diagrams for the case in which $R_0/d < 0.5$. In the transformed geometry $R_0/d = 0.45$, $R_1/d = 0.005$, $R_2/d = 0.4$. In the untransformed geometry, with homogeneous matrix, the internal relative radii of the holes are $R_1/d = 0.4$ and $R_1/d = 0.005$,

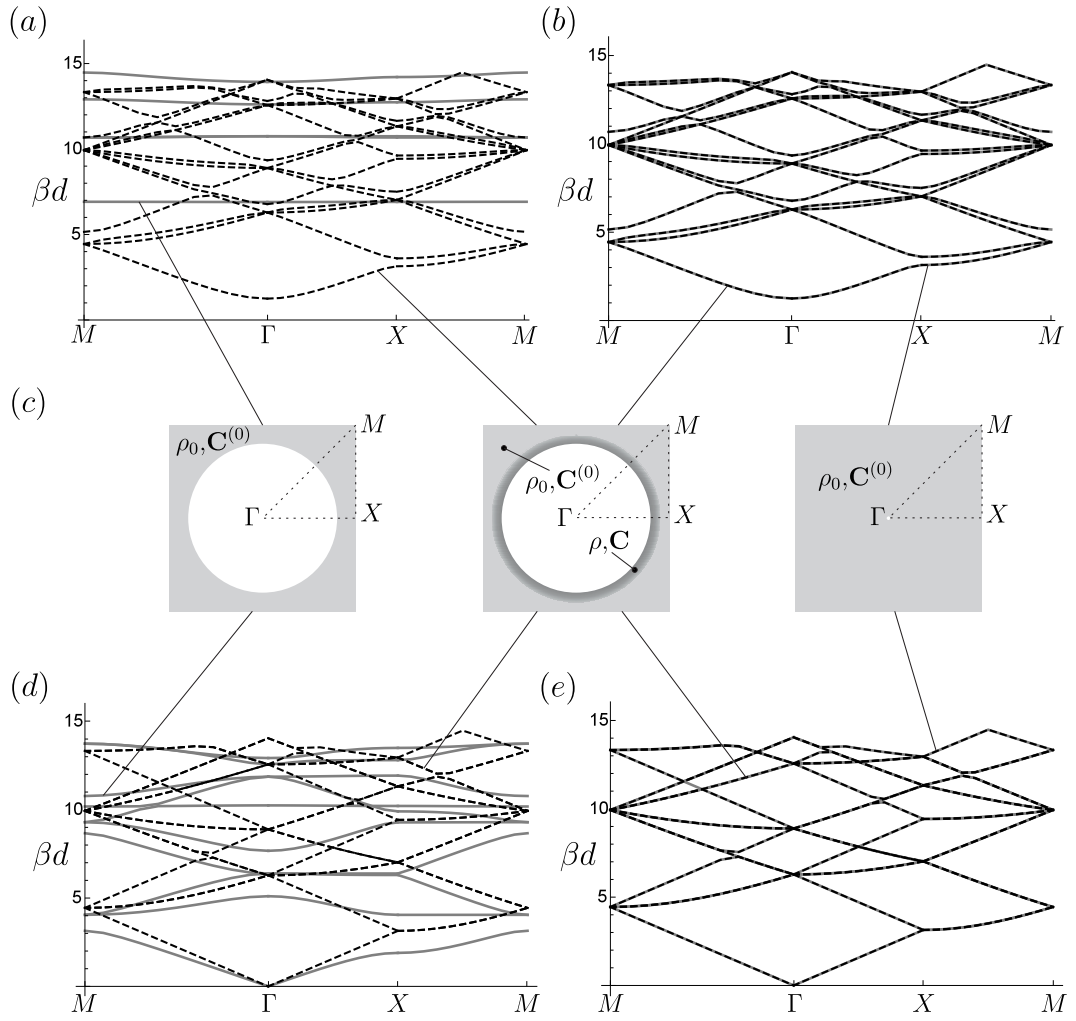

Figure 3: Dispersion diagrams. Results correspond to Dirichlet (a)-(b) and Neumann (d)-(e) boundary conditions in the central inclusions. (c) Homogeneous untransformed domains with internal radii $R_1/d = 0.4$ (left), $R_1/d = 0.005$ (right) and inhomogeneous transformed domain, with $R_0/d = 0.45$, $R_2/d = 0.4$, $R_1/d = 0.005$ (center). In the diagrams, grey continuous lines indicate untransformed geometries, dashed lines the transformed ones.

respectively. Both Neumann and Dirichlet boundary conditions are considered at the internal void boundaries. Following [45], the usual path in the reciprocal space is taken, where $\Gamma = (0, 0)$, $X = (\pi/d, 0)$, $M = (\pi/d, \pi/d)$.

It is evident that the dispersion properties for untransformed and transformed geometries with the same voids' radii $R_1/d = 0.4$ and $R_2/d = 0.4$, respectively, are strongly different. This is

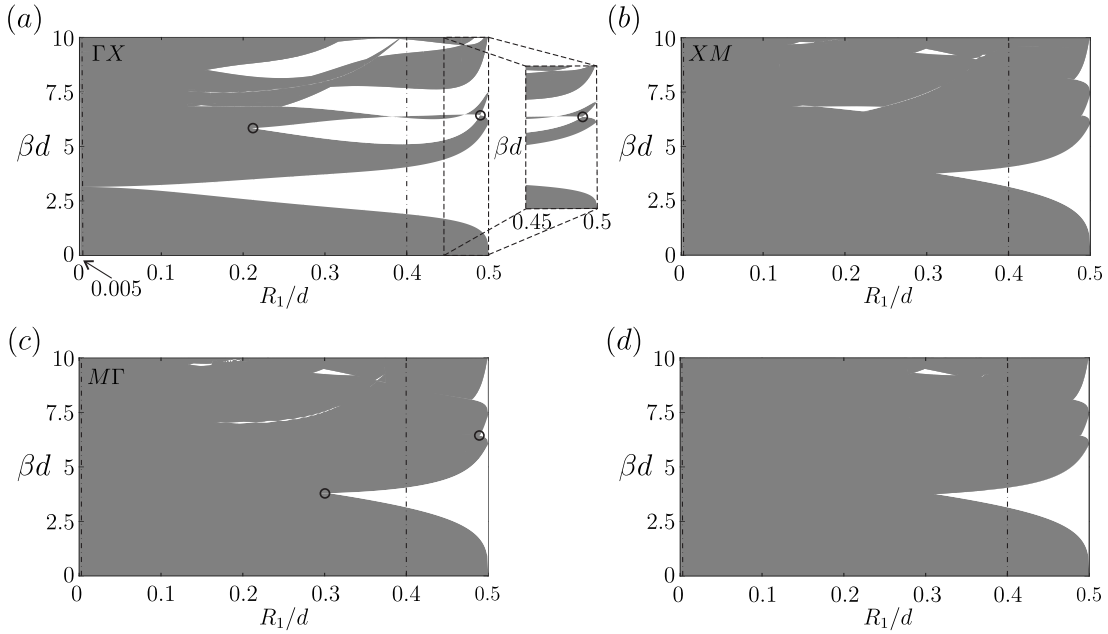

Figure 4: Band distribution of the periodic system as a function of the radius R_1/d. Grey regions are the pass bands along (a) ΓX, (b) XM, (c) $M\Gamma$ in the reciprocal space, in (d) the band distribution in the first Brillouin zone is reported. In the computation $R_0/d = 0.45$, $R_2/d = 0.4$. Some Dirac points are indicated in parts (a) and (c) with circles. The inset in part (a) shows a magnification with the Dirac point at $R_1/d = 0.489726$ and $\beta d = 6.43503$. Dot-dashed lines indicate the cases $R_1/d = 0.005$, 0.4. Video 1 in the supplementary material shows the evolution of the dispersion diagram as a function of R_1/d.

clearly associated to the distribution of the mechanical properties in the non-homogeneous shells ($R_2 \leq r \leq R_0$). On the contrary, we show on the right column the perfect match between the dispersion diagrams of the transformed geometry and the untransformed one with hole's radius $R_1/d = 0.005$. The agreement between dispersion curves for the transformed geometry and the untransformed one with $R_1/d = 0.005$ can be explained by considering the interface conditions at $r = R_0$ satisfied by the equalities (22) and that, in eqn. (23), $G(R_2) = R_1$, as imposed by the mapping (13).

Thus, we have shown that, implementing the geometric transformation detailed in Section 2.2, it is possible to mimic the dispersion properties of a periodic system with homogeneous matrix

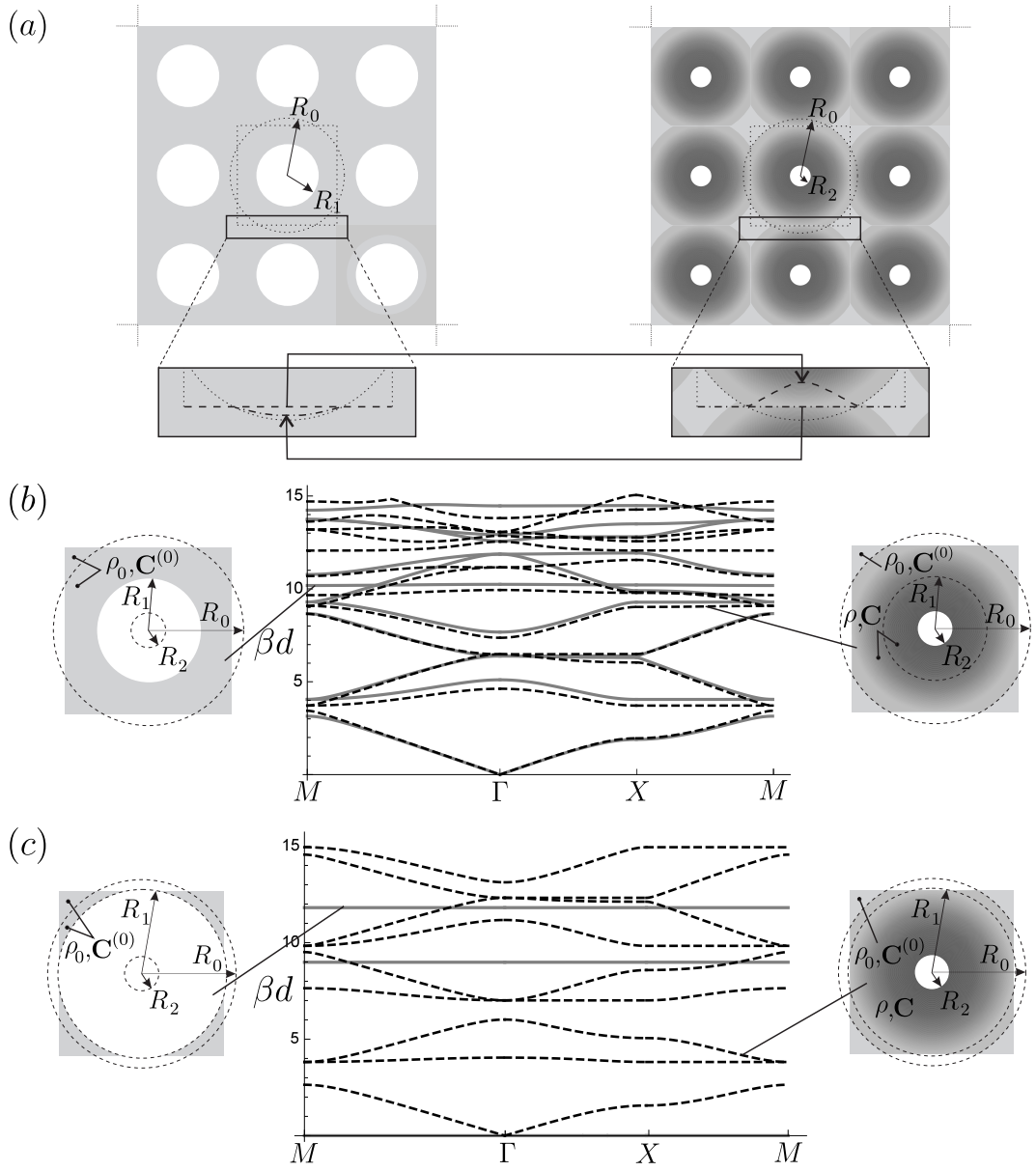

Figure 5: Overlapping transformation, $R_0 > 0.5\,d$. (a) Original and transformed geometries. In the inset the direct (11) and inverse (13) mappings of the boundaries of the central unit cell are shown in dashed and dashed-dotted lines, respectively. Dispersion diagrams for untransformed (grey lines) and transformed (black dashed lines) geometries: (b) $R_0 = 0.564\,d > 0.5\,d$, $R_1 = 0.4\,d < 0.5\,d$, $R_2 = 0.1\,d$. (c) $R_0 = 0.6\,d > 0.5\,d$, $R_1 = 0.55\,d > 0.5\,d$, $R_2 = 0.1\,d$.

having holes of internal radius R_1, with a periodic system with non-homogeneous shells with internal radius R_2.

In the second part of the work, we are going to show several applications. In particular, in Figure 4, we report the band dis-

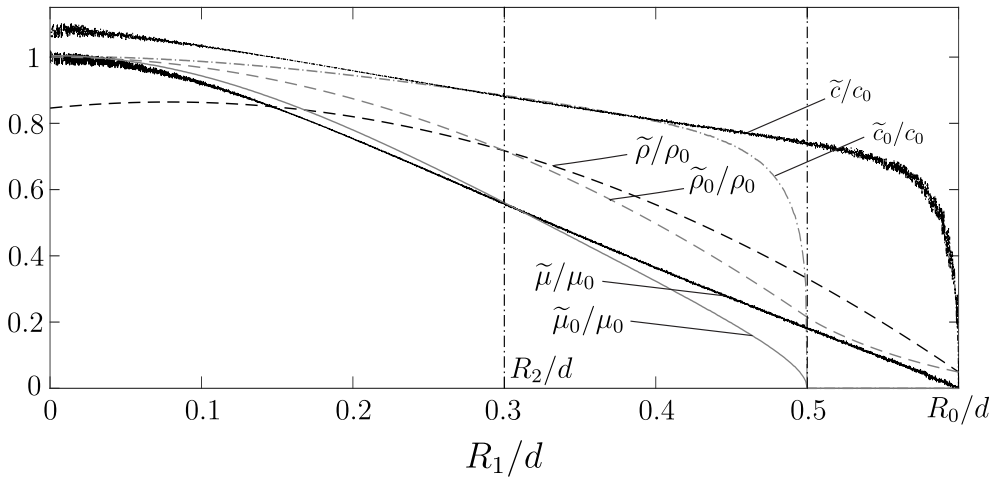

Figure 6: Effective properties in the quasi-static limit as a function of the radius R_1 (Figure 2). The effective density and shear moduli are given for the untransformed ($\widetilde{\rho}_0$ and $\widetilde{\mu}_0$) and transformed ($\widetilde{\rho}$ and $\widetilde{\mu}$) domains, together with the effective low-frequency phase velocities $\widetilde{c}$ and $\widetilde{c}_0$. The geometrical parameters $R_0 = 0.6\,d > 0.5\,d$, $R_2 = 0.3\,d$ are considered.

tribution, along the paths ΓX (a), XM (b) and $M\Gamma$ (c) and in the full first Brillouin zone (d) for Neumann boundary conditions at the voids. From the Figure we can see that, by modulating the transformation by changing the initial radius R_1, it is possible to obtain the desired filtering properties increasing the reflectance or the transmittance in a broadband frequency interval. In particular, increasing R_1 partial and full band gaps of increasing size are generated, while the second pass band for propagation along ΓX is shifted to higher frequencies when $R_1/d > 0.4$. In Section 4.1, we will show the transmitted power flow throughout an interface for two values of R_1, describing in Figure 11 different filtering effects. The dependence of the dispersion diagram on the radius R_1 can be also appreciated in Video 1 in the supplementary material.

3.2.1 The case $R_0 > 0.5\,d$. Overlapping transformations

In Figure 5 we show the comparisons between initial and transformed geometries in the case where the external radius $R_0 >$

$0.5\,d$. Two different initial geometries are considered: in part (b) $R_1 = 0.4\,d < 0.5\,d$, in part (c) $R_1 = 0.55\,d > 0.5\,d$. In the transformed geometries $R_2 = 0.1\,d$. It is evident that the dispersion diagrams show differences; this is due to the fact that the inhomogeneous shell $R_2 < r < R_0$ intersects the boundary of the unit cell and quasi-periodicity conditions are applied on two sets which are not mapped by the transformations (11) or (13). In the bottom of part (a) of Figure 5, it is possible to see the direct and inverse mapping of the boundary of the unit cell. We note from Figure 5 part (c) that, even in the case where the solid phase in the original geometry is not connected ($R_1 > 0.5\,d$), the dispersion properties of the transformed geometry maintain the 'classical' structure with stop and pass band of finite size. In particular, the local mechanical properties in the orthotropic domains are

$$\begin{aligned} \mu_r = C_{rr} &= \frac{G(r)}{G'(r)r}\mu_0 = \frac{r(R_0 - R_1) + R_0(R_1 - R_2)}{r(R_0 - R_1)}\mu_0, \\ \mu_\theta = C_{\theta\theta} &= \frac{G'(r)r}{G(r)}\mu_0 = \frac{r(R_0 - R_1)}{r(R_0 - R_1) + R_0(R_1 - R_2)}\mu_0, \end{aligned} \tag{30}$$

and

$$\rho = \frac{G'(r)G(r)}{r}\rho_0 = \frac{r(R_0 - R_1) + R_0(R_1 - R_2)}{r(R_0 - R_2)^2}(R_0 - R_1)\rho_0. \tag{31}$$

From eqns. (30) and (31), since $\min(R_2, R_0) \leq r \leq \max(R_2, R_0)$ and $\min(R_1, R_0) \leq G(r) \leq \max(R_1, R_0)$, r and $G(r)$ are always positive quantities. Thus, the positiveness of μ_r, μ_θ and ρ are governed by the factor $G'(r) = \alpha_1^{-1} = (R_0 - R_1)/(R_0 - R_2)$, which is also a positive quantity in the present and previous cases

.

We also note the interesting relation $\mu_0 = \sqrt{\mu_r \mu_\theta}$, which is mathematically analogous to the exact result $\tilde{\mu} = \sqrt{\mu_1 \mu_2}$ for the effective shear modulus $\tilde{\mu}$ of an isotropic bi-phase composite, with phase shear moduli μ_1 and μ_2, having material symmetry as, for example, a checkerboard structure. This was shown by Dykhne [18] for the conductivity problem, by making use of the 'phase interchange' relation [23, 33]. The same relation holds for the effective shear modulus of a macroscopically isotropic polycrystal, with periodically or randomly distributed microstructure, in which each anisotropic phase has principal shear moduli μ_1 and μ_2.

The effective properties in the quasi-static limit are shown in Figure 6. For the antiplane shear problem, the behavior is isotropic. The effective mass densities in the untransformed and transformed domains are

$$\tilde{\rho}_0 = \frac{1}{|\Omega^{(0,0)}_{R_1,d}|} \int_{\Omega^{(0,0)}_{R_1,d}} \rho_0 \, dA, \qquad \tilde{\rho} = \frac{1}{|\Omega^{(0,0)}_{R_2,d}|} \int_{\Omega^{(0,0)}_{R_2,d}} \rho \, dA. \tag{32}$$

The effective shear moduli have been computed by applying affine Dirichlet boundary conditions on the unit cell associated to a macroscopic strain $\tilde{\varepsilon}_{13}$ and evaluating the macroscopic stress

$$\tilde{\sigma}_{13} = \frac{1}{|\Omega^{(0,0)}_{R_i,d}|} \int_{\Omega^{(0,0)}_{R_i,d}} \sigma_{13} \, dA, \tag{33}$$

with $i = 1, 2$ in the original and transformed domains, respectively. Then,

$$\hat{\mu} = \frac{\tilde{\sigma}_{13}}{\tilde{\varepsilon}_{13}} \tag{34}$$

where $\hat{\mu}$ is $\tilde{\mu}_0$ or $\tilde{\mu}$. The effective shear modulus can be computed numerically or semi-analytically following the homogenisation scheme detailed in [11, 90].

As expected, the effective properties are not negative; $\tilde{\rho} > \tilde{\rho}_0$ and $\tilde{\mu} > \tilde{\mu}_0$ ($\tilde{\rho} < \tilde{\rho}_0$ and $\tilde{\mu} < \tilde{\mu}_0$) for $R_1 > R_2$ ($R_1 < R_2$). When $R_1/d > 0.5$, $\tilde{\mu}_0 = 0$, since the homogeneous solid phase is not connected.

The results on the transformed geometry show how it is possible to easily tune, at least in the quasi-static regime, the effective mechanical properties of the periodic system. If we compare two periodic systems with the same internal radius R_2, the first with a homogeneous solid phase and the second with a functionally graded material interface designed following the geometric transformation (13), we see that by tuning the geometrical parameter of the transformation and, in particular R_1, we can stiffen the composite ($R_1 < R_2$) or soften it ($R_1 > R_2$) up to the limit $R_1 \to R_0$, when the transformation (11) is singular and the group and phase velocities approach zero in the quasi-static limit.

3.2.2 The case $R_1 > R_0$. Unfolding transformation

We consider now an unfolding transformation corresponding to $R_1 > R_0 > R_2$. The initial and transformed geometries are shown in Figure 7, part (a), when $R_1/d < 0.5$. In the unit cell, the solid phase in the transformed geometry is homogenous for $r > R_0$ and inhomogeneous in the shell $R_2 \leq r \leq R_0$, with local properties defined as in eqns. (30) and (31). Since $G'(r)$ is now negative, the density and shear modulus are negative in the shell. The reader can now argue if it makes physical sense to have negative properties. In order to answer this question, we first follow the Veselago approach, who proposed in 1968 a theoretical model concerning the electrodynamics properties of materials with simultaneously negative dielectric permittivity and magnetic permeability [94].

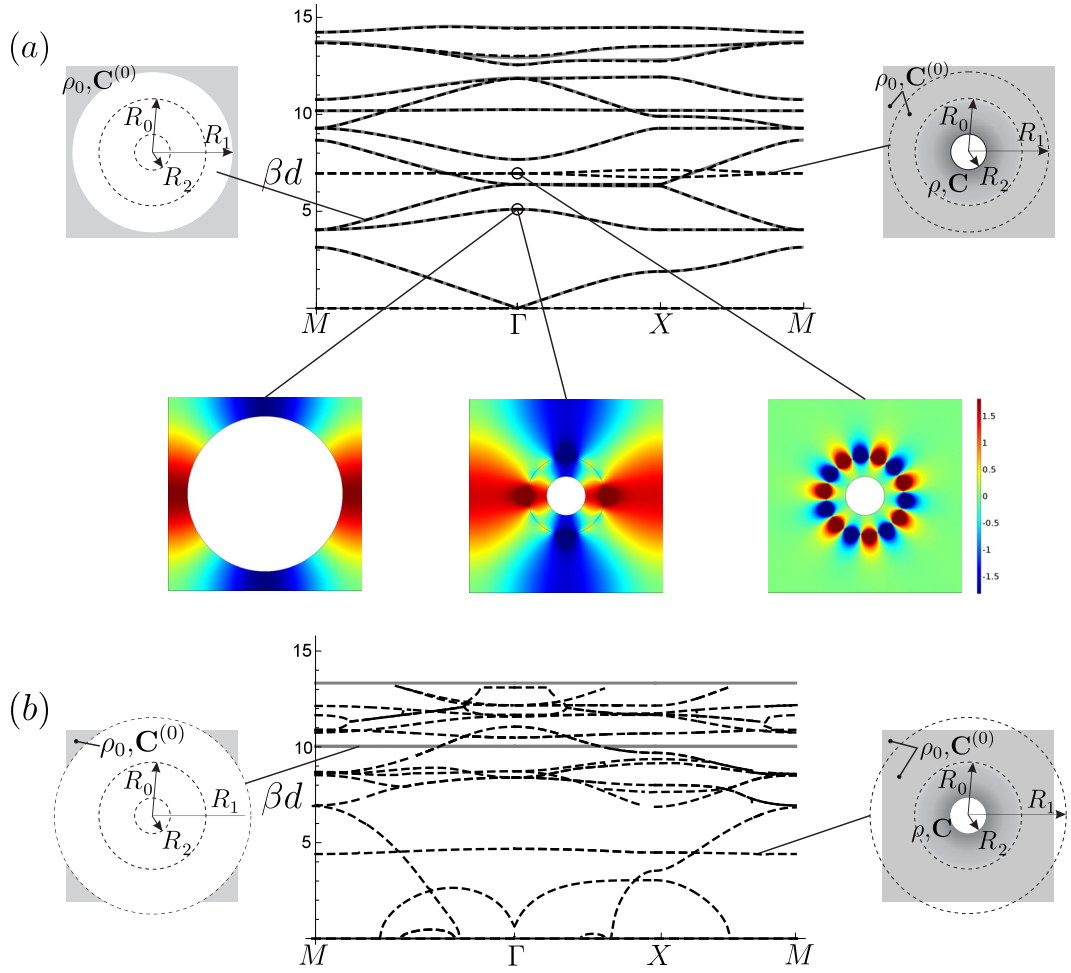

Figure 7: Unfolding transformation. Comparisons of dispersion diagrams for untransformed (grey lines) and transformed (black dashed lines) domains. (a) $R_1 = 0.4\,d < 0.5\,d$, $R_0 = 0.2\,d$, $R_2 = 0.1\,d$. (b) $R_1 = 0.564\,d > 0.5\,d$, $R_0 = 0.4\,d$, $R_2 = 0.1\,d$. Three eigenmodes are also shown in part (a). (For interpretation of the references to colour, the reader is referred to the web version of this article.)

Nevertheless, negative index materials addressed as left-handed material, backward-wave media, double negative metamaterials were proposed only after three decades [20, 75, 84]. In general relativity, the concept of negative inertial and gravitational masses is known [8]. In Newtonian mechanics a negative stiffness can be found in the incremental behavior of a nonlinear system: the snap-through mechanism is probably the simplest example of a multi-stable structural system that, due to geometric nonlinearity, may show an incremental negative stiffness in a specific range of

deformation. Alternatively, by structuring the microstructure on a scale which is small compared to the wavelength, it is possible to obtain negative properties on the mesoscale, in particular, in the dynamic regimes where internal resonances can occur [17, 39, 41].

In Figure 7 we compare the dispersion diagrams for untransformed and transformed domains. In part (a) the case $R_1 < 0.5\,d$ is reported; we note that the periodic system with inhomogeneous solid phase is capable to reproduce the same dispersion curves as the untransformed one, plus some additional ones. In the considered example, the additional curves are at $\beta d = 0$ and at the finite frequency $\beta d = 6.95$. Some of the eigenmodes at $\mathbf{k} = (0, 0)$ are also shown in Figure 7a. The two eigenmodes at $\beta d = 5.10$ have the same displacement distribution in the region $r > R_0$. In addition, for the transformed case, $u(r_A) = u(r_B)$, when $R_2 \leq r_A = g(r_B) \leq R_0$.

The eigenmode on the bottom right of Figure 7a is associated to the two additional dispersion curves at $\beta d \simeq 6.95$. It represents an anomalous localised resonance, which can be interpreted as the phononic analogous of the plasmonic resonance in electromagnetism [80]. They have been studied in electromagnetism in the quasi-static limit for a single coated inclusion [66], a square array of coated cylinders [65] and regular and disordered arrangements of coated cylinders and spheres [63]. In the quasi-static limit, Milton et al. [53, 54] have shown that the resonant field generated by a polarizable line or point dipole acts back on the polarizable line or point dipole and effectively cancels the field acting on it from outside sources. The dispersion curves for the transformed case at $\beta d \simeq 0$ confirm the quasi-static results in the literature. The analysis has been extended to consider the effect of

a finite wavelength for a single coated inclusion with homogeneous shell in [64] and numerical analyses at finite frequencies for different geometric transformations are given in [40]. In the following, we report the result of a semi-analytical approach. In order to better evidence the anomalous resonance effect, we consider the unfolding transformation on a single inclusion.

Anomalous localized resonance. A single hole of radius R_2 in a infinite domain is considered. The hole is surrounded by a non-homogeneous shell with internal radius R_2 and external one R_0. The external matrix ($r > R_0$) is homogeneous. The matrix has shear modulus μ_0 and density ρ_0, the shear modulus and the density in the shell are given by eqns. (30) and (31), with $R_2/R_0 = 0.5$ and $R_1/R_0 = 1.35 > 1$. A concentrated load

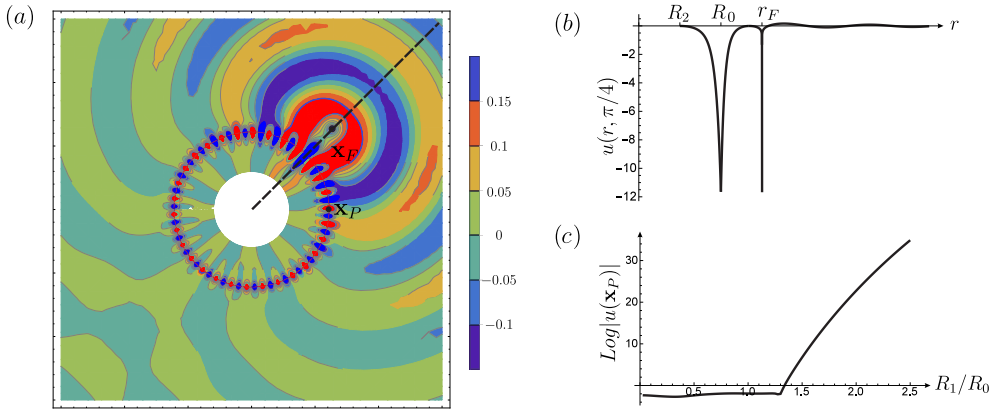

Figure 8: Anomalous localised resonance as a result of the unfolding transformation. (a) Contour plot of the displacement u is given for $R_2/R_0 = 0.5$ and $R_1/R_0 = 1.35$. (b) Displacement distribution along the dashed line indicated in part (a). (c) Displacement amplitude in the point $\mathbf{x}_P$ as a function of the ratio R_1/R_0. (For interpretation of the references to colour, the reader is referred to the web version of this article.)

is applied at $\mathbf{x}_F$, where $\mathbf{x}_F = (r_F, \theta_F)$, with $r_F = 3R_0/2$ and $\theta_F = \pi/4$, in cylindrical coordinates. The Green's function for Helmholtz equation describing the out of plane shear problem is

$$F(\hat{r}) = -\frac{i}{4} H_0^{(1)}(\beta \hat{r}), \tag{35}$$

where $\hat{r} = |\mathbf{x} - \mathbf{x}_F|$. The general solution is

$$\begin{cases} u^s(r,\theta) = \sum\limits_{n=-\infty}^{\infty} \left[A_n^s J_n(\beta\, G(r)) + B_n^s H_n^{(1)}(\beta\, G(r))\right] e^{in\theta}\,, & \text{for} \quad r < R_0\,, \\ u^m(r,\theta) = \sum\limits_{n=-\infty}^{\infty} \left[A_n^m J_n(\beta r) + B_n^m H_n^{(1)}(\beta\, r)\right] e^{in\theta}, & \text{for} \quad r > R_0\,. \end{cases} \tag{36}$$

Using the Graf's addition theorem [1], the Hankel function in eqn. (35) can be expressed as

$$H_0^{(1)}(\beta\hat{r}) = \sum_{n=-\infty}^{\infty} H_0^{(1)}(\beta r_F) J_n(\beta r) e^{in(\pi-\theta+\theta_F)}, \tag{37}$$

for $r < r_F$, leading to

$$A_n^m = 0.25\, i\, (-1)^{n+1} H_n^{(1)}(\beta r_F) e^{-in\theta_F}. \tag{38}$$

The remaining coefficients are obtained from the interface conditions

$$u^m(R_0,\theta) = u^s(R_0,\theta), \qquad \mu_0 \frac{\partial u^m}{\partial r}\bigg|_{r=R_0} = \mu\, \frac{\partial u^s}{\partial r}\bigg|_{r=R_0}, \tag{39}$$

and the Neumann boundary condition

$$\mu\, \frac{\partial u^s}{\partial r}\bigg|_{r=R_2} = 0. \tag{40}$$

They have the following expressions

$$\begin{aligned} A_n^s &= 0.25\, i\, (-1)^{n+1}\, H_n^{(1)}(\beta r_F) e^{-in\theta_F}, \\ B_n^s = B_n^m &= -\frac{J_{n+1}(\beta R_1) - J_{n-1}(\beta R_1)}{H_{n+1}^{(1)}(\beta R_1) - H_{n-1}^{(1)}(\beta R_1)} A_n^s. \end{aligned} \tag{41}$$

The real part of the displacement $u(r,\theta)$ is shown in Figure 8. In the computation, the sums in the representation (36) have been truncated at $N = 30$ and $\beta r_F = 6$. The amplitude amplification

in the neighborhood of the interface between the shell and the external matrix ($r = R_0$) is fully visible both from the contour plot in part (a) and the displacement distribution in part (b), shown along the radial line indicated in part (a) of Figure 8. In order to show the effect of unfolding in part (c) of the figure, the displacement amplitude in the point $\mathbf{x}_P = (R_0, 0)$ indicated in part (a), is given as a function of the initial radius R_1. We remember that unfolding corresponds to $R_1/R_0 > 1$. The results, in logarithmic scale, indicated an amplification on the shell-matrix interface when $R_1/R_0 \gtrsim 1.3$. We obtained an amplification at approximately the same threshold also for $\beta r_F = 12$ and $\beta r_F = 30$.

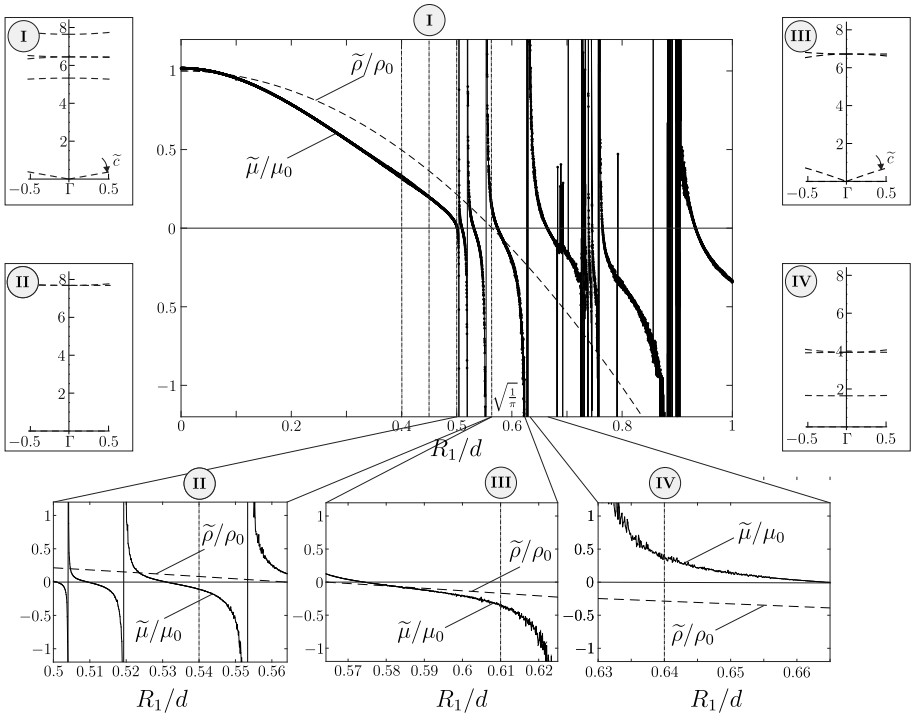

Figure 9: Low-frequency effective shear modulus and density as a function of the radius R_1. Results are given for $R_0 = 0.4\,d$, $R_2 = 0.1\,d$. Solid and dashed lines correspond to relative effective shear modulus $\widetilde{\mu}/\mu_0$ and density $\widetilde{\rho}/\rho_0$, respectively. Scaled curves are given at the bottom. The dispersion diagrams in the neighborhood of Γ are given in the four insets indicated with roman numbers **I**, **II**, **III** and **IV**; the corresponding values of R_1/d are also reported with dashed-dotted lines in the $\widetilde{\mu}/\mu_0$, $\widetilde{\rho}/\rho_0$ vs R_1/d plots.

The case $R_1 > d/2 > R_0$. The dispersion diagrams for the case of unfolding transformation, where the initial radius R_1 is greater than the half-dimension $d/2$ of the unit cell, is shown in Figure 7b. As for the case of regular transformation reported in Figure 5b, the dispersion diagrams before and after transformation are strongly different. In this case, there are additional interesting features at low-frequency. First of all, some of the branches intersect the zero frequency axis $\beta d = 0$ at finite amplitudes of the wavenumber $\mathbf{k}$ within the irreducible Brillouin zone. In prestressed flexural beams or plates such points indicate static buckling [97]; here, they are associated to anomalous internal resonance at zero frequency.

In addition, it appears that changing the initial radius R_1, it is possible to modulate the phase and group velocity in the low-frequency $\beta d \to 0$, low wavenumber $\mathbf{k} \to \mathbf{0}$ limit. In this regime, the homogenised shear modulus $\widetilde{\mu}$ and density $\tilde{\rho}$ are shown in Figure 9 as a function of the initial radius R_1, where $R_0 = 0.4\, d$ and $R_2 = 0.1\, d$. They have been computed following the procedure detailed at the end of Section 3.2.1, eqns. (32.2) and (34). In particular, when $R_0 < d/2$,

$$\tilde{\rho} = \rho_0 \left(1 - \frac{\pi R_1^2}{d^2}\right). \tag{42}$$

The results show that both $\widetilde{\mu}$ and $\tilde{\rho}$ can change in sign. Thus, there is the possibility to have propagation, when $\widetilde{\mu}/\tilde{\rho} > 0$, or no propagation, when $\widetilde{\mu}/\tilde{\rho} < 0$. Note that negative values of $\widetilde{\mu}$ and $\tilde{\rho}$ have been associated to a negative refractive index [86]. Different cases are shown in the four insets in Figure 9, indicated with the roman numbers **I**, **II**, **III** and **IV**. The dispersion curves

correspond to the different values of R_1/d, indicated with dashed-dotted lines, labelled with the same roman numbers in the effective properties plots of Figure 9. At $R_1/d = 0.45$ (case **I**) and $R_1/d = 0.61$ (case **III**), there are locally linear dispersion curves departing from Γ at $\beta d = 0$, with phase and group velocity $\tilde{c} = \sqrt{\widetilde{\mu}/\tilde{\rho}}$, since in case **I** both $\widetilde{\mu}$ and $\tilde{\rho}$ are positive and in case **III** both properties are negative. At $R_1/d = 0.54$ (case **II**) and $R_1/d = 0.64$ (case **IV**), a low-frequency finite stop band is present in the neighborhood of Γ, since $\widetilde{\mu} \lessgtr 0$ and $\tilde{\rho} \gtrless 0$ in cases **II** and **IV**, respectively. Note also that a zero frequency curve is present when $\widetilde{\mu} < 0$ or $\tilde{\rho} < 0$.

Finally, we stress that the initial radius R_1 can be used as a design parameter in order to modulate the low-frequency phase and group velocities in the neighborhood of Γ, ranging from low or zero values when $\widetilde{\mu} \to 0$ to large or unbounded ones when $\tilde{\rho} \to 0$.

4 Numerical Results

In this Section, we show possible implementations of the proposed design based on periodic transformation.

4.1 Transmission problem in an infinite medium

The transmission problem for a slab composed of three layers of inclusions surrounded by non-homogeneous shells is analysed numerically. The computational domain is shown in Figure 10a. The incident wave has the angle of incidence $\theta_I = \pi/6$, while the mechanical properties of the shells are designed following the transformation (11). In part (c) the parameters are $R_1/d = 2.2\bar{2}\cdot$

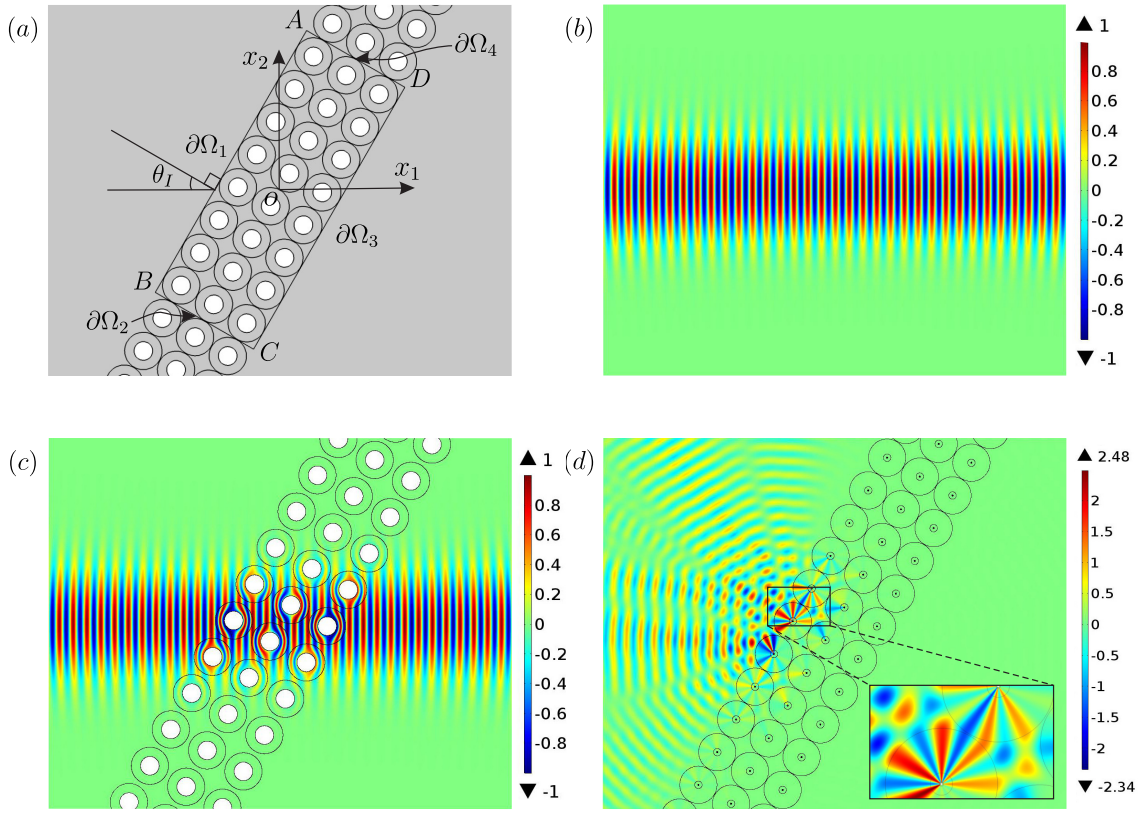

Figure 10: Transmission problem. (a) Computational domain for an oblique incident wave with angle of incidence θ_I. The interface is composed of three layers of inclusions surrounded by non-homogeneous shells. The power flux has been computed along the edges $\partial\Omega_1$, $\partial\Omega_2$, $\partial\Omega_3$ and $\partial\Omega_4$ of the rectangle $ABCD$. (b) Displacement generated by Gaussian beam in a homogeneous domain (see eqn. (43)). (c), (d) Displacement generated by a Gaussian beam interfering with the slab. The shells parameters are: (c) $R_1/d = 2.2\bar{2} \cdot 10^{-4}$, $R_2/d = 0.22\bar{2}$, $R_0/d = 0.44\bar{4}$, (d) $R_1/d = 0.44\bar{4}$, $R_2/d = 9.88 \cdot 10^{-3}$, $R_0/d = 0.494$. The size of the computational domain is $(12d \times 10d)$. (For interpretation of the references to colour, the reader is referred to the web version of this article.)

10^{-4}, $R_2/d = 0.22\bar{2}$, $R_0/4 = 0.44\bar{4}$, while in part (d) $R_1/d = 0.44\bar{4}$, $R_2/d = 9.88 \cdot 10^{-3}$, $R_0/d = 0.494$.

The numerical models have been implemented in *Comsol Multiphysics 5.3*. Details on the implementation of the numerical code are reported in Appendix B. We applied an incident Gaussian beam u_I and computed the scattered field u_S; the total field $u = u_I + u_S$ is shown in Figure 10 parts (b), (c) and (d) and Figure 1, with $\beta d = 17.2$. Non-scattering boundary conditions are imposed on the external boundary of the computational domain.

The Gaussian beam in cartesian coordinates is given by

$$u_I(x_1, x_2) = \left(1+\xi^2\right)^{-\frac{1}{4}} \exp\left[-\frac{x_2^2}{b_0^2(1+\xi^2)}\right] \exp\left[-i\left(\beta x_1 + \beta\frac{x_2^2}{2\chi} - \frac{\arctan\xi}{2}\right)\right. \tag{43}$$

where $\chi = x_1(1+\xi^{-2})$ is the radius of curvature of the beam's wavefront at x_1, $\xi = x_1/x_0$, $x_0 = \beta\, b_0^2/2$, with b_0 the beam or waist radius. In the computations, we assumed $b_0 = 1.25d$. The propagation of a Gaussian beam in a homogeneous medium is reported in Figure 10b.

In Figure 10c we show the results where the interface is an array of holes of finite size $R_2/d = 0.22\bar{2}$. The comparative results with the homogeneous case in Figure 10b show a negligible scattering produced by the interface associated to nearly full transmission. On the contrary in Figure 10d we show the results where the interface is an array of holes of negligibly small size $R_2/d = 9.88 \cdot 10^{-3}$. In such case, as a result of the design introduced by the geometric transformation, the interface is capable to reflect the incoming wave to a large extent. Thus, the slab can be designed in order to cloak the array of holes or as a full reflecting interface.

In Figure 1 we show that it is possible to obtain practically full transmission, also in the extreme case of very large holes, where $R_2/d = 0.44\bar{4}$, with $R_1/d = 2.47 \cdot 10^{-4}$ and $R_0/d = 0.494$. In the inset of the figure, it is possible to recognize from the contour plot of the displacement distribution, that the Gaussian beam can propagate in the homogeneous part of the slab practically undistorted, while in the transformed shells around each void inclusion $u(\mathbf{x}) = u(\mathcal{F}(\mathbf{X}))$.

4.1.1 Power flow

The performance in term of transmission and reflection has been assessed quantitatively by determining the power flow of the mechanical wave throughout the boundaries $\partial\Omega_i$ $(i = 1, \cdots, 4)$ of the rectangular domain $ABCD$, indicated in Figure 10a. The time-averaged (over a period $T = 2\pi/\omega$) rate of energy flux passing through a surface, with local outward normal $\mathbf{n}$, in a position $\mathbf{x}$, is [2]

$$P(\mathbf{x}) = \frac{1}{2} Re[\tau_{3j} n_j \dot{u}^*], \quad j = 1, 2\,, \tag{44}$$

where $\tau_{3j} = \mu \partial u / \partial x_j$ are the out of plane shear stress components, $\dot{u}^*$ the complex conjugate of velocity and n_j the components of the normal to the surface. Then, the power flow (per unit thickness) across each boundary $\partial\Omega_i$ $(i = 1, \cdots, 4)$, is calculated integrating the local flow per unit area as follows

$$\mathcal{P}_i = \int_{\partial\Omega_i} P ds, \tag{45}$$

where s is a local curvilinear coordinate defined in each boundary $\partial\Omega_i$. All the fluxes have been normalised by the power flow across $\partial\Omega_3$ in the homogenous case $\mathcal{P}_3^H$ (see Figure 10b), therefore

$$\hat{\mathcal{P}}_i = \frac{\mathcal{P}_i}{\mathcal{P}_3^H}. \tag{46}$$

The power flow $\mathcal{P}_3^H$ can be easily computed for a propagating Gaussian beam from the expression (43); the length of the boundary $\partial\Omega_3$ have been fixed in order to have a difference less than 1% with respect to a straight boundary $\partial\Omega_3^\infty \supset \partial\Omega_3$ of infinite length. In the following, when this condition is not satisfied, results will not be shown. The normals $\mathbf{n}_i$ to $\partial\Omega_i$ $(i = 1, \cdots, 4)$

are as follows

$$\mathbf{n}_{1,3} = (\mp\cos\theta_I, \pm\sin\theta_I)^T\,, \qquad \mathbf{n}_{2,4} = (\mp\sin\theta_I, \mp\cos\theta_I)^T\,. \tag{47}$$

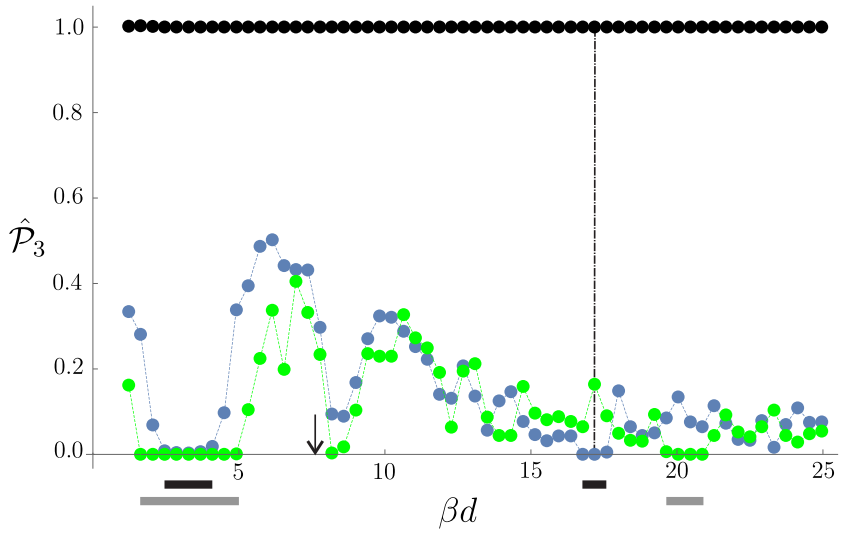

Figure 11: Rate of transmitted energy $\hat{\mathcal{P}}_3$ across $\partial\Omega_3$ as a function of the normalised frequency βd. Black dots correspond to Figure 10c, blue dots to Figure 10d, green dots to the same parameter of Figure 10d except for $R_1/d = 0.484$. The dash-dotted line corresponds to the frequency $\beta d = 17.2$ adopted in Figure 10. Thick black and grey lines at the bottom indicate the partial stop band intervals. (For interpretation of the references to colour, the reader is referred to the web version of this article.)

We identify with $\hat{\mathcal{P}}_3$ the transmitted power flow, while $\hat{\mathcal{P}}_2$ and $\hat{\mathcal{P}}_4$ give an indication of the energy radiated into the interface. The transmitted power flow $\hat{\mathcal{P}}_3$ is shown in Figure 11 as a function of the normalised frequency βd. From the black points, we note that when the small void inclusions of radius $R_1/d = 2.2\bar{2}\cdot 10^{-4}$ are mapped to the larger inclusions of radius $R_2/d = 0.22\bar{2}$ the transmitted flow $\hat{\mathcal{P}}_3 \simeq 1$ at all frequencies, meaning that the Gaussian beam can propagate within the slab practically unperturbed, in the all frequency spectrum that we have considered. On the contrary, when initial relatively large voids of radius $R_1/d = 0.44\bar{4}$ are mapped into the small voids of radius $R_2/d = 9.88\cdot 10^{-3}$ (blue dots in Figure 11), high reflectance is generated. The re-

flection is maximized in the frequency intervals corresponding to the stop bands of the periodic structure for propagation along the direction determined by the angle θ_I of the incident wave. They roughly correspond to the frequencies where $\hat{\mathcal{P}}_3 \simeq 0$. In any case, in the considered frequency spectrum, $\hat{\mathcal{P}}_3 < 0.5$. By varying the initial radius R_1, it is possible to modulate the amount of reflection; in Figure 11 we have shown in green dots the results for the case where the final geometry is the same, but the properties of the shells surrounding the voids are designed from the different initial radius $R_1/d = 0.484$. As a results, it is possible to decrease the amount of transmission with respect to the previous case (see $\beta d = 8.2$), to increase the frequency interval corresponding to negligible transmission (see $1.6 < \beta d < 4.9$), but also to shift such frequency interval (see $16.8 < \beta d < 17.6$ and $19.6 < \beta d < 20.9$).

In all the performed computations $\hat{\mathcal{P}}_2$ and $\hat{\mathcal{P}}_4$ are negligible, their moduli being always less than 10^{-5}. While they cancel each other when there is high transmission, namely $\hat{\mathcal{P}}_4 \simeq -\hat{\mathcal{P}}_2$, they are both positive when there is high reflection indicating, albeit small, some radiation into the interface.

4.2 Waveguides

In this Section, we consider out of plane elastic waves propagating along the longitudinal direction x_1 in a two dimensional waveguide of width d. The upper and lower boundaries at $x_2 = \pm d/2$ are clamped.

The propagating wave in the homogeneous waveguide has the

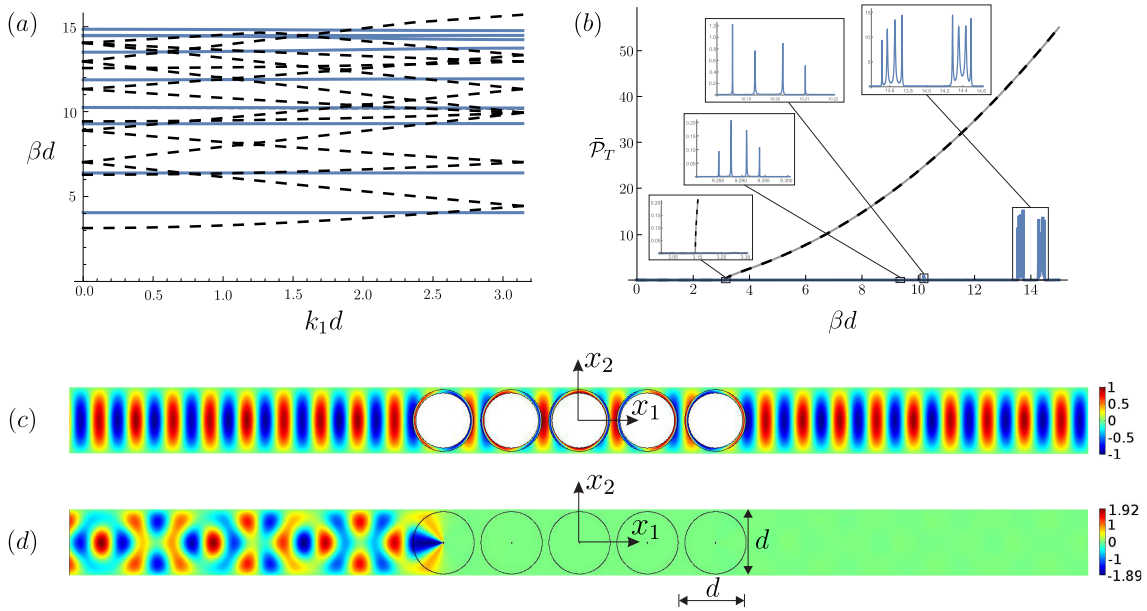

Figure 12: Wave propagation in a waveguide throughout a five units interface. (a) Dispersion relations for propagation along direction x_1. (b) Transmitted power flow $\bar{\mathcal{P}}_T = \mathcal{P}d/(c_0\mu_0)$ as a function of the normalised frequency βd. (c), (d) Out of plane displacement field for an incident wave $u_I = Re[u_1]$ (see eqn.(48)), with $\beta d = 12$. Black dashed lines and part (c) correspond to $R_1/d = 0.005$, $R_2/d = 0.4$ and $R_0/d = 0.45$, blue lines and part (d) to $R_1/d = 0.4$, $R_2/d = 0.005$ and $R_0/d = 0.45$ and the gray line in part (b) to the homogeneous waveguide. (For interpretation of the references to colour, the reader is referred to the web version of this article.)

form [51]

$$u_n(x_1, x_2) = e^{ik_1 x_1} f_n(x_2)\,, \tag{48}$$

where the real wavenumber

$$k_1 = \sqrt{\beta^2 - n^2\pi^2/d^2}, \quad n \in \mathbb{N}\,, \tag{49}$$

and

$$f_{2m-1}(x_2) = \cos\left(\frac{(2m-1)\pi x_2}{d}\right), \quad f_{2m}(x_2) = \sin\left(\frac{2m\pi x_2}{d}\right), \quad m = 1, 2, \cdot \tag{50}$$

We introduce into the waveguide a 5 units interface. Each unit has a void inclusion surrounded by a shell having material parameters defined by means of the geometric transformation (11). On the void inclusion Neumann boundary conditions

are applied, while on the upper and lower boundaries of each cell (where $\mathbf{n} = (0, \pm 1)$) Dirichlet boundary conditions are imposed.

The numerical computations have been performed in *Comsol Multiphysics 5.3*, with non reflecting boundary conditions imposed on the left and right boundaries (where $\mathbf{n} = (\pm 1, 0)$) for the transmission problem.

In Figure 12c, we consider large voids of radius $R_2/d = 0.4$. The dispersion diagram, shown in black dashed lines in part (a), approaches the dispersion diagram for a homogeneous waveguide, for which the dispersion relation satisfies eqn. (49).

For the transmission problem, we consider the incident wave

$$u_I = u_1 = e^{ik_1 x_1} \cos\left(\frac{\pi x_2}{d}\right), \tag{51}$$

with $k_1 = \sqrt{\beta^2 - \pi^2/d^2}$. Again, the wave propagates throughout the interface without any evident perturbation, showing full transmission with the shells acting as cloaking interfaces. The full transmission is detailed in Figure 12b, where the curve showing transmitted power flow in the waveguide with large voids (dashed black line) is practically coincident with the transmitted power flow in a homogeneous waveguide (grey line). In the homogeneous waveguide, following the eqns. (45) and (46), the transmitted power flow throughout a generic cross-section $x_1 = \text{const}$, is [2]

$$\mathcal{P} = \frac{\mu_0\, c_0}{4d} Re[\beta d \sqrt{(\beta d)^2 - \pi^2}], \tag{52}$$

which is positive above the cutoff frequency $\beta d = \pi$.

The opposite behavior is retrieved in Figure 12d, where the case of small voids of radius $R_2/d = 0.005$ is studied. The dis-

[2] In this case, we preferred not to show the normalised values, since in the homogenous case the power flow can be zero.

persion properties, shown in blue lines in part (a), evidence large stop bands separated by tiny pass bands, characterised by nearly horizontal dispersion curves. The transmission problem in part (d) evidences the capability of the interface to reflect the incident wave. In Figure 12b we show (in blue lines) that the reflection is maximised in the full frequency interval and to a much larger amount with respect to the continuous case analysed in Section 4.1.1. In the insets of Figure 12b, we also detailed the typical Fabry-Perot [77] resonance oscillations in correspondence of the tiny pass bands and the transmitted flow in the neighborhood of the cutoff frequency.

4.2.1 Defect modes

Here, we consider the same infinite waveguide with small voids as in Figure 12d, with an interface with units obtained employing the transformation (11), with $R_1/d = 0.4$, $R_2/d = 0.005$ and $R_0/d = 0.45$. With respect to the previous case, we do not introduce the central unit, so that the waveguide is homogeneous in the domain $(x_1, x_2) \in (-d/2, d/2) \times (-d/2, d/2)$.

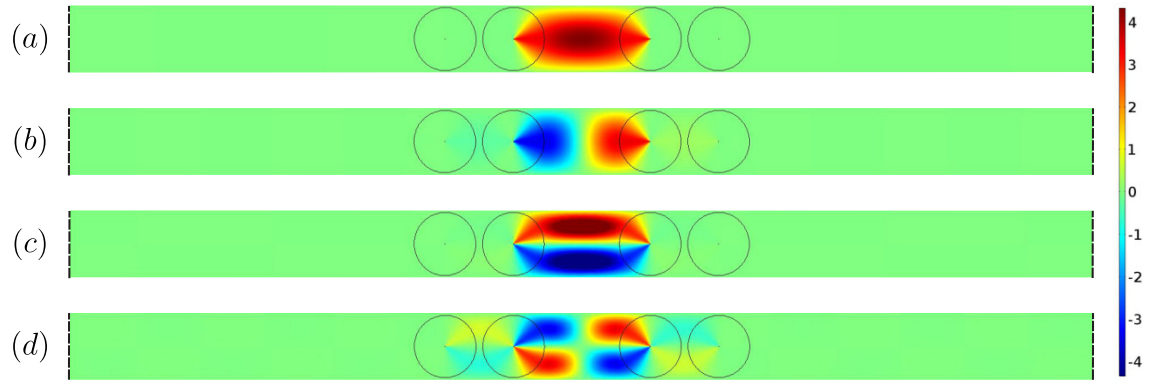

Figure 13: Defect modes in an infinite waveguide. The modes correspond to (a) $\beta d = 3.38$, (b) $\beta d = 4.40$, (c) $\beta d = 6.47$ and (d) $\beta d = 7.09$.

The infinite waveguide present a set of distinct internal res-

onance or defect modes, some of which, symmetric and skew-symmetric about the x_1 and x_2 axes, are shown in Figure 13.

These modes are generated by the inhomogeneous and anisotropic distribution of mechanical parameters designed following (11), since in a homogeneous waveguide, with the same four voids, these defect modes are not present, at last in the broad frequency interval $0 \leq \beta d \leq 15$.

4.3 Dirac Points

The dispersion diagrams for the periodic system may evidence Dirac points [38], where the system (27) displays degeneracies. From Dirac points at least two dispersion surfaces emerge as Dirac cones or Dirac-like cones [49], with finite group velocities at their vertices. The case of multiple Dirac-like cones at one Dirac point has been shown in [48]. Wave transmission at Dirac points has been associated to perfect transmission and cloaking in [5], while one-way interfacial and edge modes have been generated in elastic lattices by introducing gyroscopic spinners, which modify the topology of the dispersion diagram of the medium in correspondence of the Dirac points [25, 26]. Unidirectionally propagating waves immune to backscattering have been studied both in the frequency domain [25] and in the transient regime [26]. The dynamic behavior in the vicinity of Dirac points for elastic lattices and the associated topological phases have been recently discussed in [12, 61, 95].

In Figure 14 a Dirac point is shown. The presence of these points is associated with particular values of the initial radius R_1; the existence and the emergence of these points can be also

retrieved from the Video 1 in the Supplementary material.

Here, fixing the final geometry ($R_2/d = 0.375$, $R_0/d = 0.4$), we search for the properties in the shells $R_2 \leq r \leq R_0$ leading to Dirac points by changing the parameter R_1.

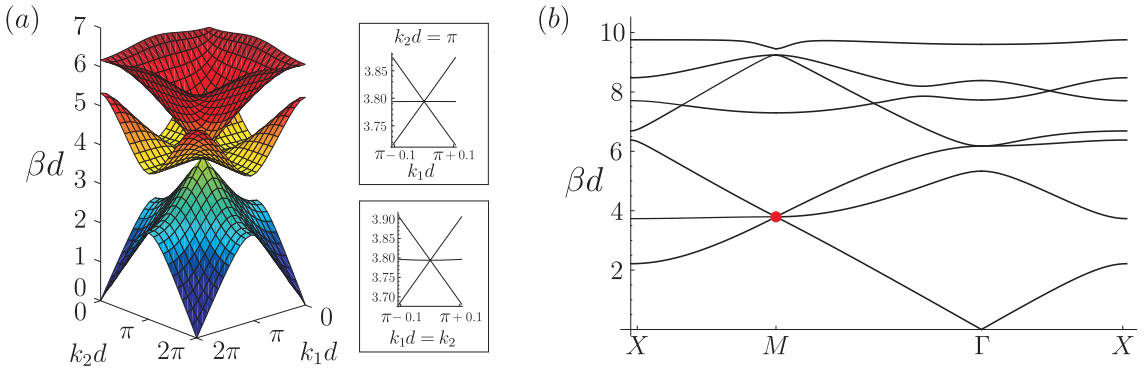

Figure 14: (a) First three dispersion surfaces with a Dirac cone at M and $\beta d = 3.79409$. (b) Dispersion diagram with Dirac point (red point). The initial radius is $R_1/d = 0.305318$. In the insets of part (a) cross sections of the dispersion surfaces are shown.

In this respect, it was convenient to make use of the multipole expansion method together with the Meylan approach [50] to find the targeted values of R_1. Dirac points are located at Γ and M in the reciprocal space. Fixing the position in the reciprocal space, we started with small values of $R_1/d = 0.005$, iterating on R_1 up to the values at which multiple eigenfrequencies were found. The coincidence of eigenfrequencies was checked up to the first 7 digits. The multipole expansion method was implemented with $N = 15$, while the Meylan method was considered by imposing close paths in the complex plane of the frequency β, centred on the positive real axis. We also checked some of the solutions obtained with the multipole expansion method with a similar implementation in *Comsol Multiphysics*; we found the same values, but we report that, in the second case, it was not always possible to find all the eigenfrequencies implementing an iterative procedure. In particular, we found that, depending on the number of eigenfrequencies

searched, the FEM package could miss some low-frequency eigensolutions.

In Figure 14b we report the dispersion diagram for $R_1/d = 0.305318$, where we indicate with a red dot the Dirac-like point at M and $\beta d = 3.794098$. A triple root of the dispersion relation (28) was found in the Dirac-like point. In part (a) of Figure 14 the first three dispersion surfaces are shown together with dispersion curves in the neighborhood of M as a function of k_1 for $k_2 = \pi$ and $k_2 = k_1$, respectively. The Dirac-like cones are evident.

R_1	$\mathbf{k}d$	βd	RM
0.211357	$\Gamma \equiv (0,0)$	5.835796	3
0.305318	$M \equiv (\pi,\pi)$	3.794098	3
0.489726	$M \equiv (\pi,\pi)$	5.429890	2
0.489726	$\Gamma \equiv (0,0)$	6.435974	3

Table 1: Degeneracies of the system (27). Initial radius R_1, normalised position in the reciprocal space $\mathbf{k}d$, normalised frequency βd and root multiplicity RM.

Finally, in Table 1 we report the values of R_1, the position in the reciprocal space, the frequencies and the multiplicity of the root solving the dispersion relation (28). Triple roots correspond to the Dirac-like points indicated in Figure 4 parts (a) and (c). At the double root at $\beta d = 5.429890$, two dispersion surfaces are tangent in a local minimum for both surfaces. Again, we stress that the transformation (11) can be tuned in order to obtain the Dirac points.

5 Conclusions

In this work we have proposed the design of a non-homogeneous periodic system derived from a periodic geometric transformation. The elastic phononic crystal merges the properties of single

inclusion cloaks via transformation optics with those of periodic systems.

Due to periodicity, it is possible to cloak an arbitrarily large region with multiple large holes, but also to obtain a highly reflective system with holes of negligible size.

The analysis of dispersive properties, typical of periodic systems, is used to quantitatively assess the dynamic properties of the elastic system after transformation. In particular, cloaking and broadband high reflection has been linked to the invariance of dispersion surfaces after transformation. The predictions based on the analysis of dispersion properties are fully confirmed by the numerical analyses for transmission problems in a continuum and in a waveguide.

Geometric transformations have been used as a design tool to determine the distribution of the mechanical parameters in the anisotropic and inhomogeneous phases of the solid as a function of the geometric parameters R_0, R_1 and R_2. For overlapping and folding transformations dispersive properties are not invariant under transformation, but lead to novel effects. Overlapping transformation can be implemented with the purpose to increase the transmission in presence of large voids, while unfolding transformations give rise to localised resonances. The low-frequency homogenisation has shown the variety of elastic behaviors that can be attained in the long wavelength regime, with the possibility to tune the effective phase and group velocities.

Final additional applications were given regarding multiple defect modes in an infinite waveguide and the tuning of transformation for the existence of Dirac points.

The transformed system is passive and does not require any ac-

tive control as in [92, 93]. In the implementation a regular transformation is used, where the initial inclusions have always a finite size and all mechanical properties are bounded. The anisotropic and inhomogeneous properties can be obtained from a lattice microstructure [14, 15] or a multilayered one [22, 57].

Acknowledgements

The financial support of the program 'Mobilità dei Giovani Ricercatori' of Università degli Studi di Cagliari is gratefully acknowledged.

References

[1] Abramowitz, M. and Stegun, I. (1965). *Handbook of mathematical functions with formulas, graphs, and mathematical tables*. New York, NY:Dover Publications.

[2] Achenbach, J. (2004). *Reciprocity in Elastodynamics*. Cambridge University Press.

[3] Alú, A. and Engheta, N. (2007). Cloaking and transparency for collections of particles with metamaterial and plasmonic covers. *Optics Express*, 15(12):7578–7590.

[4] Alù, A. and Engheta, N. (2009). Boosting molecular fluorescence with a plasmonic nanolauncher. *Physical Review Letters*, 103(4):043902.

[5] Antonakakis, T., Craster, R., and Guenneau, S. (2013). High-frequency homogenization of zero-frequency stop band photonic and phononic crystals. *New Journal of Physics*, 15(103014).

[6] Berman, C. and Greengard, L. (1994). A renormalization method for the evaluation of lattice sums. *Journal of Mathematical Physics*, 35(11):6036–6048.

[7] Bertoldi, K., Bigoni, D., and Drugan, W. (2007). Structural interfaces in linear elasticity. Part II: Effective properties and neutrality. *Journal of the Mechanics and Physics of Solids*, 55(1):35–63.

[8] Bondi, H. (1957). Negative Mass in General Relativity. *Reviews of Modern Physics*, 29(3):423–428.

[9] Brun, M., Colquitt, D., Jones, I., Movchan, A., and Movchan, N. (2014). Transformation cloaking and radial approximations for flexural waves in elastic plates. *New Journal of Physics*, 16(093020).

[10] Brun, M., Guenneau, S., and Movchan, A. (2009). Achieving control of in-plane elastic waves. *Applied Physics Lettters*, 94:061903.

[11] Brun, M., Lopez-Pamies, O., and neda, P. C. (2007). Homogenization estimates for fiber-reinforced elastomers with periodic microstructures. *International Journal of Solids and Structures*, 44(18-19):5953–5979.

[12] Chen, Y., Liu, X., and Hu, G. (2019). Topological phase transition in mechanical honeycomb lattice. *Journal of the Mechanics and Physics of Solids*, 122:54–68.

[13] Chin, S., Nicorovici, N., and McPhedran, R. (1994). Green's function and lattice sums for electromagnetic scattering by a

square array of perfectly conducting cylinders. *Physical Review*, E49(5):4590–4602.

[14] Colquitt, D., Brun, M., Gei, M., Movchan, A., Movchan, N., and Jones, I. (2014). Transformation elastodynamics and cloaking for flexural waves. *Journal of the Mechanics and Physics of Solids*, 72:131–143.

[15] Colquitt, D., Jones, I., Movchan, N., Movchan, A., Brun, M., and McPhedran, R. (2013). Making waves round a structured cloak: lattices, negative refraction and fringes. *Proceedings of the Royal Society A*, 469(2157).

[16] Craster, R. and Guenneau, S. (2012). *Acoustic Metamaterials: Negative Refraction, Imaging, Lensing and Cloaking*. Springer Series in Materials Science.

[17] Ding, Y., Liu, Z., Qiu, C., and Shi, J. (2007). Metamaterial with Simultaneously Negative Bulk Modulus and Mass Density. *Physical Review Letters*, 99(9):093904.

[18] Dykhne, A. (1971). Conductivity of a two-dimensional two-phase system. *Soviet Physics Journal of Experimental and Theoretical Physics*, 32(1):110–115.

[19] Edwards, B., Alù, A., Young, M., Silveirinha, M., and Engheta, N. (2008). Experimental verification of epsilon-near-zero metamaterial coupling and energy squeezing using a microwave waveguide. *Physical Review Letters*, 100(3):033903.

[20] Engheta, N. and Ziolkowski, R. (2006). *Metamaterials: Physics and Engineering Explorations*. Wiley & Sons.

[21] Ewald, P. (1921). Die Berechnung optischer und elektrostatischer Gitterpotentiale (Evaluation of optical and electrostatic lattice potentials). *Annalen der Physik (Leipzig)*, 369(3):253–287.

[22] Farhat, M., Guenneau, S., and Enoch, S. (2009). Ultrabroadband elastic cloaking in thin plates. *Physical Review Letters*, 103(2):024301.

[23] Flaherty, J. and Keller, J. (1973). Elastic behavior of composite media. *Communications in Pure and Applied Mathematics*, 26(4):565–580.

[24] Fleury, R. and Alù, A. (2014). Cloaking and Invisibility: a Review (Invited Review). *Progress In Electromagnetics Research*, 147:171–202.

[25] Garau, M., Carta, G., Nieves, M., Jones, I., Movchan, N., and Movchan, A. (2018). Interfacial waveforms in chiral lattices with gyroscopic spinners. *Proceedings of the Royal Society of London A*, 474:0132.

[26] Garau, M., Nieves, M., Carta, G., and Brun, M. (2019). Transient response of a gyro-elastic structured medium: Unidirectional waveforms and cloaking. *International Journal of Engineering Science*, 143:115–141.

[27] Graff, K. (1975). *Wave motion in elastic solids*. Oxford University Press, Oxford.

[28] Greenleaf, A., Lassas, M., and Uhlmann, G. (2003a). Anisotropic conductivities that cannot be detected by EIT. *Physiological Measurement*, 24(2):413–419.

[29] Greenleaf, A., Lassas, M., and Uhlmann, G. (2003b). On nonuniqueness for Calderón's inverse problem. *Mathematical Research Letters*, 10(5):685–693.

[30] Hashin, Z. (1962). The elastic moduli of heterogeneous materials. *Journal of Applied Mechanics*, 29(1):143–150.

[31] Hertz, P. (1907). Die Bewegung eines Elektrons unter dem Einflusse einer stets gleich gerichteten Kraft. *Mathematische Annalen*, 65(1):1–86.

[32] Kadic, M., Bückmann, T., Schittny, R., and Wegener, M. (2013). Metamaterials beyond electromagnetism. *Reports on Progress in Physics*, 76(12):126501.

[33] Keller, J. (1964). A theorem on the conductivity of a composite medium. *Journal of Mathematical Physics*, 5(4):548–549.

[34] Kerker, M. (1975). Invisible bodies. *Journal of the Optical Society of America*, 65(4):376–379.

[35] Kohn, R., She, H., Vogelius, M., and Weinstein, M. (2008). Cloaking via change of variables in electric impedance tomography. *Inverse Problems*, 24(1):015016.

[36] Lamb, H. (1932). *Hydrodynamics*, volume Sixth Edition. Cambridge University press.

[37] Leonhardt, U. (2006). Optical conformal mapping. *Science*, 312(5801):1777–1780.

[38] Liu, F., Lai, Y., Huang, X., and Chan, C. (2011a). Dirac cones at $\vec{k} = 0$ in phononic crystals. *Physical Review B*, 84(8):224113.

[39] Liu, X., Hu, G., Huang, G., and Sun, C. (2011b). An elastic metamaterial with simultaneously negative mass density and bulk modulus. *Applied Physics Letters*, 98(25):251907.

[40] Liu, Y., Gralak, B., McPhedran, R., and Guenneau, S. (2014). Finite frequency external cloaking with complementary bianisotropic media. *Optics Express*, 22(14):17387–17402.

[41] Liu, Z., Zhang, X., Mao, Y., Zhu, Y., Yang, Z., Chan, C., and Sheng, P. (2000). Locally Resonant Sonic Materials. *Science*, 289(5485):1734–1736.

[42] Lueg, P. (1990). On the invention of active noise control. *The Journal of the Acoustical Society of America*, 87:2251–2254.

[43] MacKenzie, J. (1950). The elastic constants of a solid containing spherical holes. *Proceedings of the Physical Society B*, 63(1):2–11.

[44] Mansfield, E. (1953). Neutral holes in plane sheet-reinforced holes which are elastically equivalent to the uncut sheet. *The Quarterly Journal of Mechanics and Applied Mathematics*, 6(3):370–378.

[45] Maurin, F., Claeys, C., Deckers, E., and Desmet, W. (2018). Probability that a band-gap extremum is located on the irreducible Brillouin-zone contour for the 17 different plane crystallographic lattices. *International Journal of Solids and Structures*, 135:26–36.

[46] Maxwell, J. (1890). *On physical lines of force*. The Scientific Papers of James Clerk Maxwell ed W D Niven (Cambridge: Cambridge University Press).

[47] McPhedran, R., Movchan, A., and Movchan, N. (2009). Platonic crystals: bloch bands, neutrality and defects. *Mechanics of Materials*, 41(4):356–363.

[48] McPhedran, R., Movchan, A., Movchan, N., Brun, M., and Smith, M. (2015). Parabolic trapped Modes and Steered Dirac Cones in Platonic Crystals. *Proceedings of the Royal Society A*, 471(2177):20140746.

[49] Mei, J., Wu, Y., Chan, C., and Zhang, Z. (2012). First-principles study of Dirac and Dirac-like cones in phononic and photonic crystals. *Physical Review B*, 86(3):035141.

[50] Meylan, M. and Gross, L. (2003). A parallel algorithm to find the zeros of a complex analytic function. *Australia and New Zealand Industrial and Applied Mathematics Journal*, 44(E):E236–E254.

[51] Miklowitz, J. (1978). *The Theory of Elastic Waves and Waveguides*, volume 22. North Holland Publishing Company, Amsterdam.

[52] Milton, G., Briane, M., and Willis, J. (2006). On cloaking for elasticity and physical equations with a transformation invariant form. *New Journal of Physics*, 8:248.

[53] Milton, G. and Nicorovici, N.-A. (2006). On the cloaking effects associated with anomalous localized resonance. *Proceedings of the Royal Society A*, 462(2074):3027–3059.

[54] Milton, G., Nicorovici, N.-A., McPhedran, R., K.Cherednichenko, and Jacob, Z. (2008). Solutions in

folded geometries, and associated cloaking due to anomalous resonance. *New Journal of Physics*, 10(11):115021.

[55] Milton, G. and Willis, J. (2007). On modifications of Newton's second law and linear continuum elastodynamics. *Proceedings of the Royal Society A*, 463(2079):855–880.

[56] Misseroni, D., Movchan, A., and Bigoni, D. (2019). Omnidirectional flexural invisibility of multiple interacting voids in vibrating elastic plates. *Proceedings of the Royal Society A*, 475(20190283).

[57] Morini, L. and Gei, M. (2019). Waves in one-dimensional quasicrystalline structures: dynamical trace mapping, scaling and self-similarity of the spectrum. *Journal of the Mechanics and Physics of Solids*, 119:83–103.

[58] Moroz, A. (2006). Quasi-periodic Green's functions of the Helmholtz and Laplace equations. *Journal of Physics A*, 39(36):11247–11282.

[59] Movchan, A., Movchan, N., and McPhedran, R. (2007). Bloch-Floquet bending waves in perforated thin plates. *Proceedings of the Royal Society A*, 463(2):2505–2518.

[60] Muskhelishvili, N. (1949). *Some Basic Problems of the Mathematical Theory of Elasticity*. Groningen, P.Noordhoff, Ltd.

[61] Nanthakumar, S., Zhuang, X., Park, H., Nguyen, C., Chen, Y., and Rabczuk, T. (2019). Inverse design of quantum spin hall-based phononic topological insulators. *Journal of the Mechanics and Physics of Solids*, 125:550–571.

[62] Nelson, P. and Elliott, S. (1992). *Active control of sound*. Academic Press.

[63] Nicorovici, N.-A., McKenzie, D., and McPhedran, R. (1995). Optical resonances of three-phase composites and anomalies in transmission. *Optics Communications*, 117(1-2):151–169.

[64] Nicorovici, N.-A., McPhedran, R., Enoch, S., and Tayeb, G. (2008). Finite wavelength cloaking by plasmonic resonance. *New Journal of Physics*, 10(11):115020.

[65] Nicorovici, N.-A., McPhedran, R., and Milton, G. (1993). Transport properties of a three-phase composite material: the square array of coated cylinders. *Proceedings of the Royal Society A*, 442(1916):599–620.

[66] Nicorovici, N.-A., Mcphedran, R., and Milton, G. (1994). Unusual Resonant Phenomena where Image Charges have a Real Significance. *Physical Review B*, 49.

[67] Noginov, M., Li, H., Barnakov, Y., Dryden, D., Nataraj, G., Zhu, G., Bonner, C., Mayy, M., Jacob, Z., and Narimanov, E. (2010). Controlling spontaneous emission with metamaterials. *Optics Letters*, 35(11):1863–1865.

[68] Norris, A. (2008). Acoustic cloaking theory. *Proceedings of the Royal Society A*, 464(2097):2411–2434.

[69] Norris, A., Amirkulova, F., and Parnell, W. (2012). Source amplitudes for active exterior cloaking. *Inverse Problems*, 28:105002.

[70] Norris, A., Amirkulova, F., and Parnell, W. (2013). Active elastodynamic cloaking. *Mathematics and Mechanics of Solids*, 19(6):603–625.

[71] Norris, A. and Shuvalov, A. (2011). Elastic cloaking theory. *Wave Motion*, 48(6):525–538.

[72] Norris, A. and Vemula, C. (1995). Scattering of flexural waves on thin plates. *Journal of Sound and Vibration*, 181(1):115–125.

[73] O'Neill, J., Selsil, O., McPhedran, R., Movchan, A., and Movchan, N. (2015). Active cloaking of inclusions for flexural waves in thin elastic plates. *The Quarterly Journal of Mechanics and Applied Mathematics*, 68(3):263–288.

[74] Pendry, J. (2000). Negative refraction makes a perfect lens. *Physical Review Letters*, 85(18):3966–3969.

[75] Pendry, J., Holden, A., Stewart, W., and Youngs, I. (1996). Extremely Low Frequency Plasmons in Metallic Mesostructures. *Physical Review Letters*, 76(25):4773–4776.

[76] Pendry, J., Schurig, D., and Smith, D. (2006). Controlling electromagnetic fields. *Science*, 312(5781):1780–1782.

[77] Perot, A. and Fabry, C. (1899). On the application of interference phenomena to the solution of various problems of spectroscopy and metrology. *Astrophysical Journal*, 9(16):87–115.

[78] Poulton, C., McPhedran, R., Movchan, N., and Movchan, A. (2010). Convergence properties and flat bands in platonic

crystal band structures using the multipole formulation. *Waves in Random and Complex Media*, 20(4):702–716.

[79] Poulton, C., Movchan, A., McPhedran, R., Nicorovici, N., and Antipov, Y. (2000). Eigenvalue problems for doubly periodic elastic structures and phononic band gaps. *Proceedings of the Royal Society A*, 456(2002):2543–2559.

[80] Raether, H. (1988). *Surface Plasmon on smooth and rough surface and grating*. Springer-Verlag, Berlin.

[81] Rayleigh, L. (1892). On the influence of obstacles arranged in rectangular order upon the properties of medium. *Philosophical Magazine*, 34(211):481–502.

[82] Raza, M., Liu, Y., Lee, E., and Ma, Y. (2016). Transformation thermodynamics and heat cloaking: a review. *Journal of Optics*, 18(4):044002.

[83] Sarychev, A. and Shalaev, V. M. (2007). *Electrodynamics of Metamaterials*. World Scientific.

[84] Shelby, R., Smith, D., and Shultz, S. (2001). Experimental Verification of a Negative Index of Refraction. *Science*, 292(5514):77–79.

[85] Silveirinha, M. and Engheta, N. (2006). Tunneling of electromagnetic energy through subwavelength channels and bends using ϵ-near-zero materials. *Physical Review Letters*, 97(15):157403.

[86] Smith, D., Pendry, J., and Wiltshire, M. (2004). Metamaterials and Negative Refractive Index. *Science*, 305(5685):788–792.

[87] Smith, M., Meylan, M., and McPhedran, R. (2011). Scattering by cavities of arbitrary shape in an infinite plate and associated vibration problems. *Journal of Sound and Vibration*, 330(16):4029–4046.

[88] Smith, M., Meylan, M., and McPhedran, R. (2013). Flexural wave filtering and platonic polarizers in thin elastic plates. *The Quarterly Journal of Mechanics and Applied Mathematics*, 66(4):437–463.

[89] Smith, M., Meylan, M., McPhedran, R., and Poulton, C. (2014). A short remark on the band structure of free edge platonic crystals. *Waves in Random and Complex Media*, 24(4):421–430.

[90] Suquet, P. (1990). Une methode simplifié pour le calcul des propriétés élastiques de matériaux hétérogénes a structure périodique. *Comptes Rendue de l'Académie des Sciences Seriés*, 311(2b):769–774.

[91] Vasquez, F., Milton, G., and Onofrei, D. (2009a). Active exterior cloaking for the 2D Laplace and Helmholtz equations. *Physical Review Letters*, 7(103):073901.

[92] Vasquez, F., Milton, G., and Onofrei, D. (2009b). Broadband exterior cloaking. *Optics Express*, 7(17):14800–14805.

[93] Vasquez, F., Milton, G., and Onofrei, D. (2011). Exterior cloaking with active sources in two dimensional acoustics. *Wave Motion*, 48:515–524.

[94] Veselago, V. (1968). The electrodynamics of substances with

simultaneously negative values of ϵ and μ. *Soviet Physics Uspekhi*, 10(4):509–514.

[95] Xia, B., Wang, G., and Zheng, S. (2019). Robust edge states of planar phononic crystals beyond high-symmetry points of Brillouin zones. *Journal of the Mechanics and Physics of Solids*, 124:471–488.

[96] Zalipaev, V., Movchan, A., Poulton, C., and McPhedran, R. (2002). Elastic waves and homogenization in oblique periodic structures. *Proceedings of the Royal Society A*, 458(2024):1887–1912.

[97] Ziegler, H. (1956). On the Concept of Elastic Stability. *Advances in Applied Mechanics*, 4:351–403.

Appendix A. Comparison between multipole expansion method and finite element simulations

To determine the dispersion surfaces, we fixed the wave vector $\mathbf{k}$ and we searched for the frequency β satisfying the dispersion relation (28). In the multipole expansion method, we implemented the Meylan approach [50], searching for the number of roots within a closed path in the complex plane of β. The paths are centred on the positive real axis and in the analysis we have found only real values.

A comparison between the frequencies computed in *Comsol Multiphisics* and the semi-analytical multipole expansion approach is reported in Table 2. In the computations N is the truncation

number adopted for the finite system (27), approximating the infinite sum in (26), which we have taken equal to the truncation number for the sum in h_1 and h_2 in (25).

$\mathbf{k}d$	FEM	ME ($N=2$)	ME ($N=5$)	ME ($N=10$)
$\left(\frac{\pi}{2},0\right)$	1.356952	1.358036	1.356951	1.356952
	4.526865	4.532874	4.526868	4.526865
	6.257810	–	6.257825	6.257810
	6.559204	6.849747	6.559220	6.559201
	7.929420	7.938114	7.929743	7.929421
	8.037572	8.136470	8.037584	8.037570
$\left(\pi,\frac{\pi}{2}\right)$	2.714203	2.714191	2.714200	2.714203
	3.754604	3.773696	3.754605	3.754604
	5.127843	5.204680	5.127832	5.127841
	7.348258	7.369042	7.348285	7.348258
	7.989113	–	7.989165	7.989111
	8.804243	8.383524	8.804280	8.804240
$\left(\frac{\pi}{2},\frac{\pi}{2}\right)$	1.948120	1.948065	1.948119	1.948120
	4.337816	4.343927	4.337814	4.337816
	5.378690	5.498149	5.378691	5.378688
	7.539204	7.588725	7.539273	7.539201
	7.544650	7.854300	7.545151	7.544664
	8.435667	8.574477	8.435700	8.435666

Table 2: Comparison between numerical (FEM) and multipole expansion (ME) methods. The first 6 eigenfrequencies βd have been computed at three different points in the reciprocal space. Values correspond to a transformed geometry with $R_0/d = 0.4$, $R_1/d = 0.3$, $R_2/d = 0.375$ ($\alpha_1 = 0.25$). Neumann boundary conditions are applied at $r = R_2$. In the multipole expansion method the system (26) and the sum in h_1 and h_2 in (25) have been truncated at $N = 2$, $N = 5$ and $N = 10$, respectively.

Appendix B. Finite element implementation of the transmission problem

Details on the implementation of the finite element simulation are given here. The most problematic numerical computation was the one reported in Figure 10d, where $R_1/d = 0.44\bar{4}$, $R_2/d = 9.88 \cdot 10^{-3}$, $R_0/d = 0.494$. Around each void of radius R_2 we built three shell domains, with external radii $2R_2$, $10R_2$ and R_0,

respectively. In each domain, from the inner to the outer, we set the maximum element size s_E/d equal to $1.23 \cdot 10^{-4}$, $2.47 \cdot 10^{-3}$ and $9.88 \cdot 10^{-3}$, respectively, while in the external matrix the limiting element size is $s_E/d = 1.23 \cdot 10^{-2}$. The mesh consists of $9.2 \cdot 10^6$ linear triangular elements corresponding to $64.5 \cdot 10^6$ degrees of freedom. The computation was performed on a 2xXeon E5-2600v4 workstation with 192 GB RAM in 57 min.